Contrasts in two- and three-dimensional system behaviour in the modelling of compositionally originating LLSVPs and a mantle featuring dynamically obtained plates

S.M. Langemeyer[1], J.P. Lowman[2], P.J. Tackley[3]

[1]Department of Physics, University of Toronto, Toronto M5S 1A7, Canada
[2]Dept. of Physical and Environmental Sciences, University of Toronto Scarborough, Toronto, M1C 1A4, Canada
[3]Department of Earth Sciences, ETH-Zurich, Sonneggstrasse 5, 8092 Zurich, Switzerland

Running Title:

Modelling LLSVPs and plates in mantle convection models

Corresponding author: Julian Lowman, julian.lowman@utoronto.ca

SUMMARY More than two decades of systematic investigation has made steady progress towards generating plate-like surface behaviour in models of vigorous mantle convection. Accordingly, properties required to obtain dynamic plates from mantle convection have become widely recognized and employed in both 2D and 3D geometries. Improving our understanding of the properties required to obtain durable (or replenishable) deep mantle features with LLSVP-like characteristics has received interest for a period with similar longevity. Investigation ultimately focusses on discovering the properties able to produce the presence of a detached pair of three-dimensional features, distinct from the ambient mantle. Here, we assume the LLSVPs have a chemical origin by incorporating a Compositionally Anomalous and Intrinsically Dense (CAID) mantle component comprising 2-3.5% of the total mantle volume. The feedback between plate formation and the presence of a CAID mantle component is investigated in both 2D and 3D spherical geometries. We explore the impact of both an intrinsic contrast in density and viscosity for the CAID component, with the objective of finding system parameter values that encourage the formation of a pair of LLSVP-like assemblages and a surface that exhibits the principle features of terrestrial plate tectonics; including recognizable and narrowly focussed divergent, convergent and (in 3D) transform plate boundaries that separate 8-16 distinct plate interiors. We present the results of nine two-dimensional and eleven three-dimensional calculations and show that for some of the cases examined, a pair of CAID material provinces can be freely obtained in two-dimensional cases while maintaining a surface characterized by plate-like behaviour. However, specifying the same system parameters in the three-dimensional model does not readily yield a pair of enduring provinces for any values of the parameters investigated. Moreover, the inclusion of the CAID component in the mantle can affect the global geotherm so that in comparison to the surface behaviour obtained for the initial condition isochemical model, the surface behaviour of the cases incorporating the dense component are less exemplary of plate tectonics. In general, CAID material components that are 3.75%-5% denser than the surrounding mantle (at surface temperatures), and up to a factor of 100 times greater in intrinsic viscosity, form layers populated by voids, or nodes connected by tendril-like ridges that reach across the core-mantle-boundary, rather than distinct piles resembling LLSVPs. Due to its inherently heavy and stiff character, in equilibrated systems, we find the CAID material becomes especially hot so that the temperature-dependence of its density and viscosity results in reduced distinction between the intrinsically dense assemblages and the ambient mantle. Accordingly, the CAID material forms masses on the CMB that are relatively less dense (0.625%-1.5%) and viscous than the adjacent mantle material, in comparison to the percentage differences obtained at common temperatures. We find that by adjusting our yield stress model to account for the influence of the CAID material on the geotherm, a highly satisfactory plate-like surface can be re-attained, however, the formation of a pair of LLSVP-shaped masses remains elusive.

keywords:

convection currents, and mantle plumes; composition and structure of the mantle;

dynamics of lithosphere and mantle; mantle rheology; mantle processes

1 Introduction

The Large Low Shear-wave Velocity Provinces (LLSVPs) observed below Africa and the Pacific Ocean (Ritsema et al., 1998; Ni et al., 2002; To et al., 2005; Garnero & McNamara, 2008; Hernlund & Houser, 2008; Auer et al., 2014) comprise first order physical features in the lower mantle. Evidence that supports an at least partial chemical origin for the LLSVPs includes seismic observations of broadly spanning velocity-magnitude anomalies and the sharp shear-wave velocity gradient boundaries that confine these regions (Ritsema et al., 1998; Ni et al., 2002; To et al., 2005; Garnero & McNamara, 2008; Lekic et al., 2012). However, the inferred densities of the volumes encompassed within the LLSVPs vary. Evidence from the analysis of solid Earth tides (Lau et al., 2017) permits density anomaly excess of little more than a half percent in the LLSVPs, relative to the adjacent mantle. The Stonely modes of free oscillation data (Koelemeijer et al., 2017) suggest that the provinces are less dense overall than the surrounding mantle, despite their deep location. Such findings may hint at LLSVP evolution that is consistent with marginally stable, chemically dense but relatively hot, transient sluggish masses (Li et al., 2019) rising from the core mantle boundary (CMB). In any case, the conflicting observations add to the uncertainty in resolving the physical parameters responsible for the LLSVPs (e.g., McNamara, 2019). Indeed, several studies have shown that the morphology of the seismically slow provinces might be explained by thermal anomalies in isochemical models (Schuberth et al., 2009, 2012; Davies et al., 2015). However, although arguments for purely thermal origins for the LLSVPs are credible, the observation of an anticorrelation between bulk sound and shear modulus (Su & Dziewonski, 1997; Ishii & Tromp, 1999; Masters et al., 2000; Trampert et al., 2004; Moulik & Ekström, 2016) makes a compositional origin for the LLSVPs a compelling hypothesis. Accordingly, thermochemical modelling of the evolution of the deep mantle requires obtaining discrete compositionally originating piles on the CMB that spend at least part of their existence coalesced into a pair of roughly diametrically opposed, steep-sided, hot but intrinsically dense provinces. Moreover, the detached chemically distinct volumes comprising the piles may reach over a thousand kilometres in height above the CMB (Cottaar & Lekic, 2016).

The longevity of this arrangement may exceed several mantle transit times (the time required for a parcel of mantle material to traverse the depth of the mantle at the mean velocity of the plates). Previous studies have concluded that the LLSVPs have occupied their current positions for several hundred million years (Burke & Torsvik, 2004; Dziewonski et al., 2010; Torsvik et al., 2010). The location of large igneous provinces (LIPs) suggests a correlation with the peripheries of the LLSVPs which have been argued to be the site of plume generation zones (PGZs) formed by the influence of a sharp lateral temperature gradient at the edges of thermochemical provinces (Torsvik et al., 2006; Burke et al., 2008; Li & Zhong, 2017; Heyn et al., 2020). Given this connection, the age and positioning of the LIPs suggests that the LLSVPs are both stable and relatively immobile (at least some of the time) for periods in excess of 200 Myr. However, intermittent mobility of the LLSVPs, as well as changes in their morphology, in response to plate motion and subduction zone migration is evident in thermochemical convection studies that have imposed plate reconstruction histories as surface boundary conditions (McNamara & Zhong, 2005; Zhang et al., 2010; Flament et al., 2017). These studies have incorporated intrinsically dense components that produce a pair of LLSVP-configuration provinces in response to the imposition of an evolving plate velocity field that agrees with inferred records for the past 200+ Myr and speculative histories extending back hundreds of millions of years before that. Although two current-day LLSVP-type thermochemical features can be obtained on the CMB when recent plate history is simulated, it is not clear that broad chemically distinct provinces on the CMB can be obtained when full feedback between a thermochemical mantle component and the plates is modelled.

Adhering to the hypothesis that the LLSVPs are compositional in nature (Humayun et al., 2004; Tackley et al., 2005; Boyet & Carlson, 2006; Labrosse et al., 2007; Deschamps et al., 2011), we investigate the feedback between a dynamically evolving plate-like surface velocity field in two- and three-dimensional thermochemical mantle convection models and the distribution of a compositionally anomalous and intrinsically dense (CAID) component introduced into the deep mantle of vigorously convecting systems (e.g., Trim et al., 2014; Trim & Lowman, 2016; Stein et al., 2020). With plates being absent, previous findings (e.g., Hansen & Yuen, 1989; Tackley, 1998; LeBars & Devaille, 2004; McNamara & Zhong, 2004; Li et al., 2014; Tan et al., 2011) demonstrated the ability of a compositionally dense mantle component to aggregate into a small number of stable piles that may interact with the ambient mantle by responding to downwelling flow or influencing upwelling location. The primary controlling influence over pile durability and longevity is the contrast in density between the ambient and enriched mantle. In addition, pile stability and morphology has been shown to be dependent on the thermally derived viscosity contrast within the convecting system (Li et al., 2014) as well as the intrinsic viscosity contrast between the ambient mantle and CAID material (McNamara & Zhong, 2004; Heyn et al., 2018). The rheological properties of a compositionally distinct component comprising the LLSVPs is not known but it has been proposed that the LLSVPs are either enriched in Bridgmanite and iron (Trampert et al., 2004) or depleted of ferropericlase (Yamazaki & Karato, 2001). Given that an absence of interconnected regions of lower viscosity ferropericlase would have a lower viscosity than a nearly pure Bridgmanite component (Ballmer et al., 2017), it may be that the LLSVPs are inherently more viscous than the material in the surrounding mantle.

Due to feedback, the simultaneous modelling of dynamically obtained plates and an intrinsically dense component in the deep mantle is a problem that is distinct from the modelling of either a system that features compositionally dense piles while lacking plates or the obtaining of a plate-like surface over-lying an interior where dense provinces are absent. For example, previous studies have shown that, when they form, dense piles become mobile or susceptible to breakup as a result of the impact of slab-like downwellings (Hansen and Yuen, 1989; McNamara & Zhong, 2005; Langemeyer et al., 2020). Plate-like surface characteristics produce especially focussed sheet-like downwellings and can also have a strong effect on heat flow and the temperature profile of the mantle (Lowman et al., 2001); potentially changing the requirements for pile formation. Similarly, the presence of compositional provinces influences heat flow (Amit & Olson, 2015; Li et al., 2018; Langemeyer et al., 2020) at the core mantle boundary (CMB), altering the thermal profile of the system and therefore a property upon which the obtaining of a plate-like surface behaviour strongly depends (e.g., Stein & Hansen, 2008). Accordingly, the addition of a CAID component to a mantle convection model exhibiting self-consistently generated plates can, potentially, result in the cessation of the plate behaviour (Trim et al., 2014). Moreover, LLSVP-emulating provinces can influence the positioning of thermal plumes which, in turn, can disrupt the stability of the plates and the quiescence of their interiors. However, the converse is similarly applicable. The inclusion of CAID material in the convecting system has the potential to be the ingredient that alters the thermal field in a way that can allow plates to form when other system parameters would otherwise not be conducive to their generation. Determining the physical requirements for the generation of plates and LLSVP-like compositionally originating provinces is thus a problem that simultaneously requires satisfying two requirements influenced by the same parameters.

Recognizing that the existence of plate tectonics and the LLSVPs are distinct but coupled features simultaneously required by a global mantle convection model presents constraints and the potential for discovering limits on the composition of the LLSVPs. A small number of studies of the dynamic interaction between these two first-order features at the surface and base of the mantle have been presented (Trim et al., 2014; 2016) but continued investigation may provide important further insight into important physical mechanisms governing the Earth's evolution. For example, two-dimensional modelling has shown that the formation of a pair of CAID material provinces with LLSVP-type morphologies is not guaranteed by the inclusion of a dense component in a fully dynamic model, but that two stable, non-transient, piles can be obtained if the CAID material has specific qualities (Langemeyer et al., 2018, 2020; Li et al., 2019). Previous studies (Trim et al., 2016) have also shown that when a small number (1-3) of durable provinces are obtained, they can be as mobile on the CMB as continents on the surface. Understanding whether CAID material provinces are inherently stationary or prone to episodic bouts of translation also requires modelling in conjunction with the existence of dynamic plates.

In this study we further investigate the feasibility of and requirements for distributing a compositionally anomalous component of the mantle into two distinct and detached large provinces. Previous work employing two-dimensional calculations (Langemeyer et al., 2020) showed that in systems featuring self-consistently evolving plates, the formation of a small number (i.e., 1-3) of provinces was just one possible outcome for the distribution of a dense component comprising between 3 and 5% of the mantle's volume. Following the examples of previous studies, these authors varied both the relative intrinsic density and viscosity of the dense mantle component (e.g., Heyn et al., 2018; Li et al, 2014; Deschamps & Tackley, 2008) and found that specific combinations of these parameters were conducive to producing a durable and persistent pair of provinces that yielded periods in which LLSVP-like topographic profiles were obtained. (Alternative formations of the dense components range from a basal layer to multiple lower-volume piles.) In this study, we continue the approach of the previous work by first examining the influence of the stress-dependence of the lithosphere's rheology on the formation of the plate boundaries and the distribution of the CAID material in two-dimensional calculations and, subsequently, we model full 3D spherical shell systems featuring evolving plates and an intrinsically dense component.

2 Methods

2.1 Governing Equations

Thermochemical convection is modelled in a spherical geometry using a finite volume code (Tackley, 2000) for solving the dimensionless equations of mass, momentum and energy conservation in a bi-modally heated infinite Prandtl number Boussinesq fluid. Advection of the compositional field is calculated using the tracer-ratio method (Tackley & King, 2003). Thus, we specify

$$\nabla \cdot \mathbf{u} = 0 \tag{1}$$

$$\nabla \cdot [\eta(\nabla \mathbf{u} + (\nabla \mathbf{u})^T)] - \nabla P = (-\mathrm{Ra_T} T + \mathrm{Ra_c} C)\hat{r} \tag{2}$$

$$\frac{\partial T}{\partial t} = \nabla^2 T - \mathbf{u} \cdot \nabla T + \mathrm{H} \tag{3}$$

and

$$\frac{\partial C}{\partial t} = -\mathbf{u} \cdot \nabla C \tag{4}$$

where $\mathbf{u}$ is velocity, η is dynamic viscosity, P is the non-hydrostatic pressure, T is temperature, t is time, H is the non-dimensional internal heating rate, $\mathrm{Ra_T}$ is the reference thermal Rayleigh number, $\mathrm{Ra_C}$ is the compositional Rayleigh number and C is the compositional field. The compositional field tracks the distribution of the intrinsically dense material such that $0 \leq \mathrm{C} \leq 1$ and the value of C gives the ratio of the mass of the CAID material to the total mass, per unit volume. A region featuring a compositional value of $C = 1$ is entirely comprised of enriched material, while $C = 0$ represents the ambient mantle. Equations (1) - (4) have been non-dimensionalised utilizing a thermal diffusion timescale. Furthermore, $\eta = \bar{\eta}/\eta^*$, where $\bar{\eta}$ is the dimensional field and η^* is the dimensional reference viscosity.

The thermal Rayleigh number and compositional Rayleigh number are defined as:

$$\mathrm{Ra_T} = \frac{\rho_0 g \alpha \Delta T d^3}{\kappa \eta^*} \tag{5}$$

and

$$\mathrm{Ra_C} = \frac{\Delta \rho_C g d^3}{\kappa \eta^*}, \tag{6}$$

where ρ_0 is the reference density defined as $\rho_0 = \rho(T_0)$, α is the thermal expansivity, d is the thickness of the mantle, $\Delta T = T_b - T_0$ is the difference between the superadiabatic isothermal basal temperature (T_b) and the isothermal surface temperature (T_0), g is acceleration due to gravity, $\Delta \rho_C$ is the contrast in density between intrinsically dense and ambient mantle material and κ is the thermal diffusivity.

The contrast in the Rayleigh numbers is described by the value of the buoyancy number $\mathrm{B} = \mathrm{Ra_C}/\mathrm{Ra_T} = \Delta \rho_C/(\rho_0 \alpha \Delta T)$ (representing the relative influence of thermal and compositional effects on the density of the mantle material). For example, with a buoyancy number of 0.5 the Boussinesq approximation results in an enriched mantle component at a non-dimensional temperature of 0.5 having the same density as the ambient mantle at a non-dimensional temperature of 0.0. (In general, for constant thermal expansion coefficient, $\rho(T = \mathrm{B}, C = 1.0) = \rho(T = 0.0, C = 0.0)$).

The governing equations (1) - (4) are thus completed by the incorporation of a linearized equation of state

$$\rho(T, C) = \rho_0[1 + \alpha \Delta T(\mathrm{B}C - T)]. \tag{7}$$

The non-dimensional internal heating rate is defined as:

$$H = \frac{\rho_0 \epsilon d^2}{k \Delta T} \tag{8}$$

Table 1. Dimensional quantities adopted for this study.

Quantity	Dimensional Value
η^*	4.5×10^{19} Pa · s
κ	1×10^{-6} m^2 s^{-1}
d	2.89×10^6 m
ΔT	2500 K
diffusion time, d^2/κ	265 Gyr
ρ_0	3700 kg m^{-3}
g	10 m s^{-2}
α	2×10^{-5} K^{-1}
k	4.3 W m^{-1} K^{-1}

where ϵ is the dimensional heating rate per unit mass (specified here as uniform throughout the mantle) and k is the thermal conductivity. The dimensional values corresponding to the reference Rayleigh number and assumed in the dimensional interpretation of the results are provided in Table 1.

2.2 Rheology

A mobile surface is attained through the implementation of a temperature-dependent viscosity combined with viscoplastic yielding. The viscosity temperature-dependence is specified using a non-dimensional Arrhenius-type law, where

$$\eta_T = \exp\left(\frac{E_a}{T+1} - \frac{E_a}{2}\right) \tag{9}$$

where E_a is a non-dimensional activation energy, determining the magnitude of the viscosity contrast due to temperature alone, between material at the surface and the core mantle boundary (CMB). This study uses a set value of $E_a = 29.96$ to generate a thermal viscosity contrast, ΔT, of 3.2×10^6.

A non-dimensional yield stress, σ_{yield}, is implemented by prescribing a surface yield stress value, σ_{surf}, and a mantle yield stress value, σ_{mantle}, that defines the yielding point below a prescribed non-dimensional depth, d_l. The prescribed depth-dependent yield stress is

$$\sigma_{\text{yield}} = \min[\sigma_{\text{mantle}}, \sigma_{\text{surf}} + \frac{D(\sigma_{\text{mantle}} - \sigma_{\text{surf}})}{d_l}], \tag{10}$$

where D is a non-dimensional depth below the model surface and d_l is the depth below which the mantle is prescribed a fixed yield stress value of σ_{mantle}.

We incorporate plastic yielding by utilizing a linearly proportional relationship between yield stress and yield viscosity, such that

$$\eta_{\text{yield}} = \frac{\sigma_{\text{yield}}}{2\dot{\epsilon}} \tag{11}$$

where $\dot{\epsilon}$ is the second invariant of the strain rate tensor, $\sqrt{\frac{1}{2}\dot{\epsilon_{ij}}\dot{\epsilon_{ij}}}$.

In addition to the influences of temperature and stress, the variation in the rheological behaviour of the system is augmented by the inclusion of a specified increase in lower mantle viscosity. A number of geophysical observables have inferred an increase in mantle viscosity by a factor of 30 or greater at a depth corresponding to the phase transition from spinel to Bridgmanite + magnesiowüstite (Boehler, 2000; Hager, 1984; Richards & Hager, 1984; King & Masters, 1992; Mitrovica & Forte, 2004). Therefore, we specify an increase in lower mantle viscosity so that

$$\eta_{\text{TD}} = \eta_{\text{T}} \times \eta_{\text{D}}, \tag{12}$$

where

$$\eta_{\text{D}} = 1 \quad \text{for} \quad z \geq 1 - 0.227 \quad \text{and} \quad \eta_D = 30 \quad \text{for} \quad z \leq 1 - 0.227, \tag{13}$$

where z represents the non-dimensional height above the core mantle boundary with $z = 1 - 0.227$ corresponding to a dimensional depth of 660km.

To account for the impact on viscosity of temperature, depth and stress dependence, we define a composite viscosity that considers the relative importance of the contributing influences

$$\eta_{\rm comp} = 1/[1/\eta_{\rm TD} + 1/\eta_{\rm yield}]. \tag{14}$$

The final effect on viscosity, specifically explored in this study, is the specification of an intrinsic viscosity contrast owing to composition, $\Delta\eta_{\rm c}$. The two component fluid has a viscosity given by $\eta_{\rm comp} \times (\Delta\eta_{\rm c})^C$, where C is the local value of the composition field.

2.3 Thermal steadiness

In this study, we vary $\Delta\eta_{\rm c}$, the buoyancy number, B, the yield-stress value as a function of depth and the volume of the intrinsically dense component in the systems. All cases featuring a CAID material component are initiated from snapshots taken from statistically steady systems that feature no CAID component. Details of the initial conditions are given in the following section. The calculations incorporating CAID material are each a continuation of the calculation used to obtain the initial condition, with the addition of a uniform thickness layer of CAID material enveloping the core at the start of the new experiment. Subsequently, these new systems converge to statistically steady states themselves.

Calculations are considered to have reached a statistically steady-state when heat flow from the surface is balanced by the sum of the heat flow from the core to the mantle and the internally generated heat. Specifically, a steady-state is considered to be established when the time-averaged non-dimensional internal heating rate (set to 30 in all calculations) is equal to the difference in non-dimensional heat flows:

$$\frac{3(F_s - F_b f^2)}{1 + f + f^2}, \tag{15}$$

where F_s and F_b are the mean non-dimensional surface and basal heat fluxes and f is the ratio of core to planetary radius (we specify a terrestrial value of 0.547 in this study). Convergence to a temporally averaged steady-state condition is obtained for the initial condition used in both the 2D and 3D calculations.

3 Results

3.1 Yield stress and model dimension

We first consider the behaviour of two-dimensional systems with a uniform non-dimensional yield stress of 2×10^7 (110 MPa). Previously, Langemeyer et al. (2020) described the evolution of two-dimensional calculations featuring a yield stress of 1×10^7 in otherwise identical systems. However, employing the same values for the system parameters, Langemeyer et al. (2021) showed that in isochemical three-dimensional systems, a uniform yield stress of 2×10^7 results in a more plate-like surface behaviour, with time-dependent boundaries that commonly exhibit Earth-like structure; namely, the appearance of spreading boundaries comprised of divergent segments and transform-like offsets coexisting with contrasting arcuate convergent boundaries. The primary objective of the study presented here is to examine the feedback between plate-like surface behaviour and a CAID component in the lower mantle, and to gain insight into any differences arising from the system dimensionality. Accordingly, we employ the higher yield stress in all calculations by first re-examining the behaviour of 2D systems. In later sections we present 3D calculations featuring a CAID component with other system parameter values matching those employed by Langemeyer et al. (2021).

The impact of the higher yield stress is to reduce the number of surface weak zones associated with subduction and divergence. The distribution of CAID material and the internal thermal structure are affected. As in the previous two-dimensional modelling work (Langemeyer et al., 2020) the buoyancy number of the CAID material as well as its viscosity relative to the ambient material are both varied, in order to determine their influence on the distribution of the CAID material.

We introduce a naming convention to simplify the discussion. Model names follow the format #DBbbDdd, where bb is the buoyancy number of the intrinsically dense material, dd is the contrast in viscosity between ambient and intrinsically dense material (at the same temperature and depth), represented as a multiplicative factor, and # is the number of dimensions used in the calculation. For example a three-dimensional calculation featuring a buoyancy number of 0.85 and a CAID material intrinsic viscosity that is a factor of 10 times greater than the viscosity of the ambient mantle material is designated: Model 3DB0.85D10.

3.2 Initial condition

Figure 1 shows the initial condition fields used for all 2D calculations presented. Corresponding temperature and viscosity are shown and reveal a pair of distinct downwellings. The initial condition is generated using an isochemical model. The surface features spreading centres and downwelling generating zones of focussed plate convergence, while the base

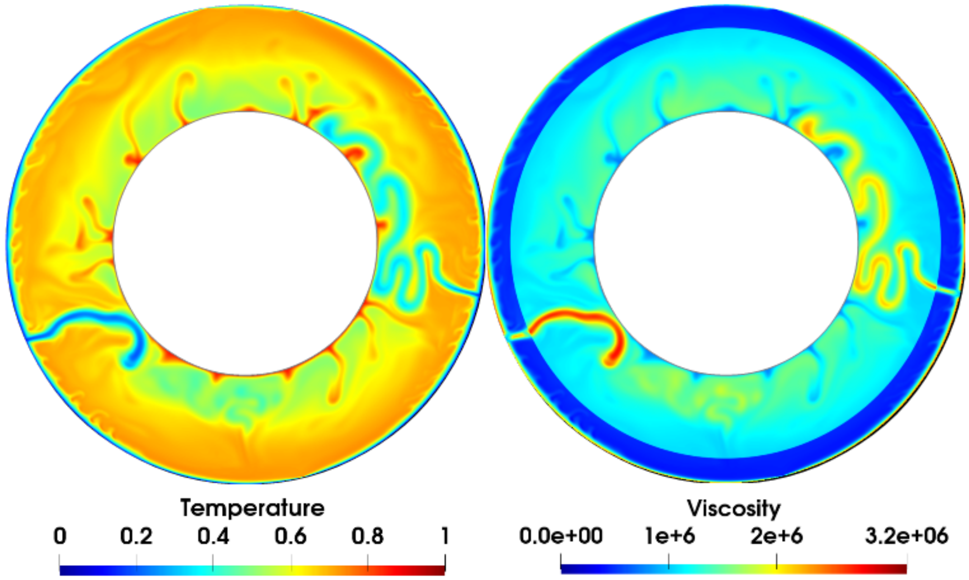

Figure 1. The initial condition non-dimensional temperature and viscosity fields used for all 2D calculations presented in this study. All two-dimensional calculations presented are obtained for a spherical annulus geometry with a resolution of 128 × 1024. The CAID material advection is modelled with the tracer ratio method (Tackley & King, 2003) using approximately 4.2 million tracers in each case.

of the mantle produces multiple active upwellings. The 2D calculations presented in the remainder of this study are initiated by adding a uniform height layer of CAID material enveloping the CMB, into the fields shown in Fig. 1. The evolution of this material is then analysed with time 0.0 corresponding to the initial condition.

3.3 Distribution of the CAID material in 2D calculations

Figure 2 shows temperature and composition field snapshots from nine calculations in which all parameters are identical, with the exception of the buoyancy number of the CAID material and its viscosity relative to the ambient mantle ($\Delta\eta_C$). The CAID material comprises 3.5% of the mantle volume in all calculations. The snapshots show the presence of either one or two downwellings that are formed by surface convergence at a high-stress originating weak zone. In general, these downwellings persist for approximately one to several mantle transit times before waning. Upwellings forming in regions devoid of CAID material, as well as on top of CAID provinces, lack the vigour to reach the base of the plates. For cases where $\Delta\eta_c = 1$ or 10, upwellings commonly occur at the edges or highest elevation points of the dense provinces. In cases where $\Delta\eta_c = 100$ upwelling formation is often coincident with the points of highest elevation above CAID material piles. Regardless of the location of upwelling formation, at no point are upwellings observed to impinge upon the lower lithosphere.

Throughout the evolution of these calculations the intrinsically denser component is often distributed into one large pile with intermittent episodes characterized by the formation of two piles (often diametrically opposed). The cases shown exhibit a single pile (with small secondary piles in some cases) when $\Delta\eta_c \geq 10$ or 100. In contrast, two diametrically opposed piles are common when $\Delta\eta_c = 1$. We also find that a pair of diametrically opposed piles of similar size are often present early in model evolution (e.g., in Models 2DB0.75D100 and 2DB1.0D100), but eventually a single pile is formed. In general, when the intrinsic viscosity of the CAID material is lower, transient piles tend to collapse and spread over the CMB following interaction with downwellings that push the dense component into high structures. As the intrinsic viscosity contrast, $\Delta\eta_C$ is increased, events leading to compression, and to higher and less wide piles (e.g., due to the impact of neighbouring downwellings), leave longer-lived signatures in stiffer piles. An inverse trend is also observed between the buoyancy number and the height of CAID material piles so that cases with a buoyancy number of 0.75 typically feature greater height piles than cases with a buoyancy number of 1.0. A potential impact on the dynamics responsible for the formation of the plates results from a decrease in the relative viscosity of the CAID material (e.g., when it is hot and not intrinsically higher in viscosity) or an increase in buoyancy number. Both factors lead to an increase in CMB blanketing by the dense component. Increased coverage of the CMB can lead to a cooler mantle in comparison to an isochemical case. For example, a blanketing layer, or discrete piles, can inhibit heat flow from the core. As a result, mean global viscosity is affected by both the buoyancy number and the intrinsic viscosity of the CAID material and, in turn, a resulting difference in plate behaviour can determine the number of downwellings able to form and therefore whether CAID material disperses into one or more piles. In summary, the findings from our 2D calculations indicate that a higher intrinsic viscosity for the CAID material promotes degree-1 mantle flow, especially for cases with reduced buoyancy ratio.

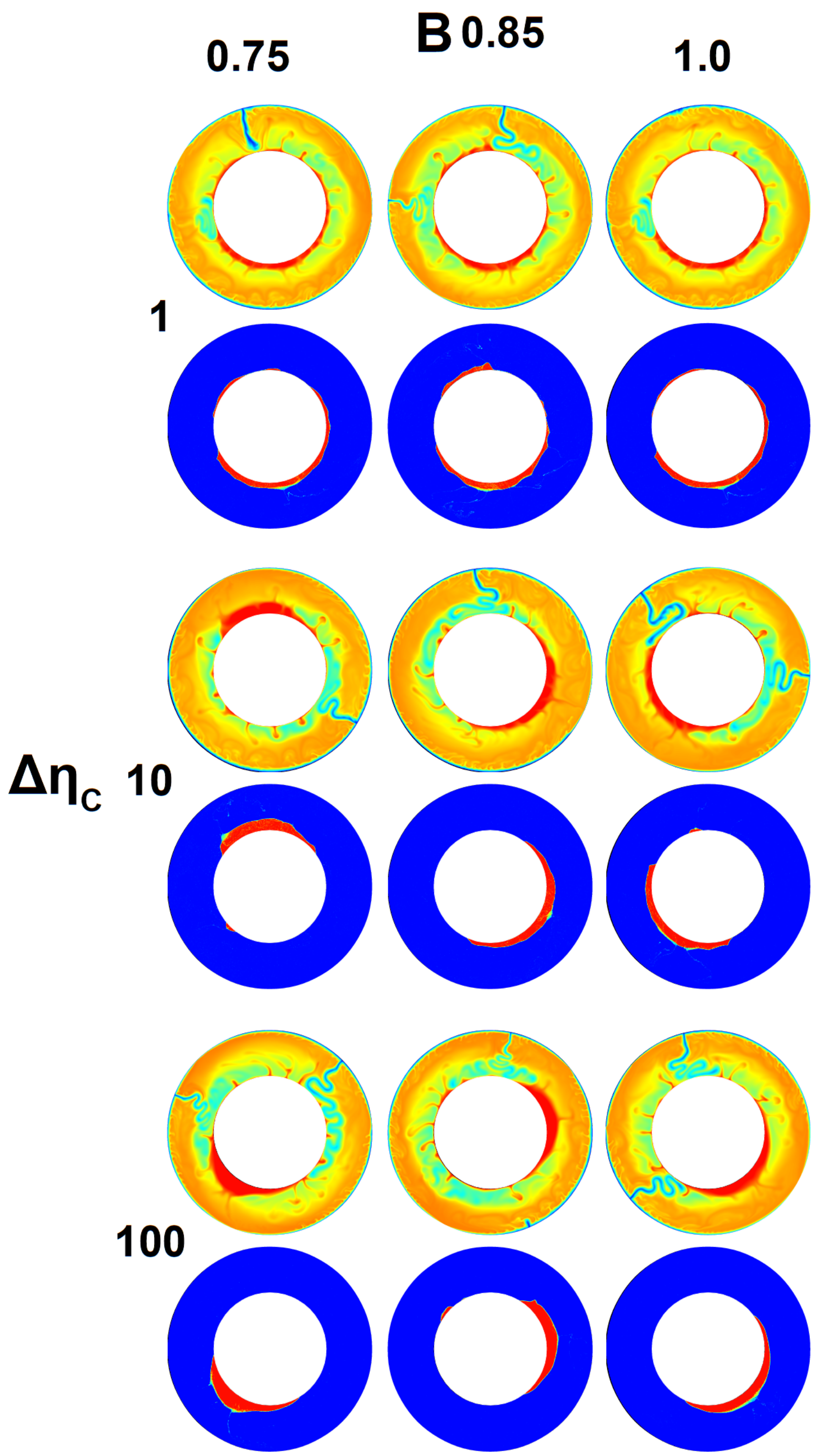

Figure 2. Temperature (top) and composition (bottom) field snapshots featuring a range of buoyancy numbers (columns) and CAID material intrinsic viscosities (rows). The temperature scale is the same as in Fig. 1. Red and blue in the composition fields correspond to values of 1.0 and 0.0, respectively.

3.4 Thermal state time-dependence and CAID material distribution

Figure 3 presents snapshots of the thermal and compositional fields from Models 2DB0.75D100 and 2DB0.75D10, as well as basal and surface heat flux time series for the three cases from Fig. 2 featuring a buoyancy number of 0.75. In general, mean heat flux is minimally influenced by the intrinsic viscosity of the CAID material, however, variation between maximum and minimum surface heat flux values is reduced when there is no intrinsic contrast in viscosity between the different compositions (most likely because the predominantly degree-one-flow cases are more impacted by the opening and closing of a smaller number of plate boundaries). Red and blue vertical lines are annotated on the heat flux time series, indicating the timing of the snapshots shown. Both times are selected for their relation to a spike in surface heat flux, which occurs following the transition from a system with a single downwelling to periods featuring the development of a new surface weak zone (resulting in the formation of second downwellings that supersede the existing downwellings which subsequently dissipate). Pre-existing long lasting downwellings appear in the southern and northern hemispheres for cases 2DB0.75D100 and 2DB0.75D10, respectively, while young downwellings are seen to form in the northern and southern hemispheres in the same cases. For case 2DB0.75D100 it is observed that mean surface heat flux increases by approximately 21 mW/m^2 following the initiation of a downwelling in the northern hemisphere. The basal heat flux is observed to have a similar response to the development of new downwellings. However, throughout the period modelled, the basal heat flux varies over a narrower range of values with a slightly delayed response.

Sudden variations in heat flux associated with the development and loss of surface downwelling regions indicate the transient nature of these calculations. A similar frequency in the rate of heat flux variation is observed for all three cases presented in Figure 3 with each case experiencing at least one rapid increase in surface heat flux per Gyr, indicating the formation of a new zone of convergence forms in the calculations at intervals of 1 Gyr or less. Generally, changes in the amplitude of the heat flux time variations also coincide with changes in the nature of the CAID material's distribution due to the feedback between the surface motion and intrinsically dense component.

Figure 4 is similar to Figure 3, but illustrates the evolution of cases where $\Delta\eta_c = 100$. For reference, Model 2DB0.75D100 appears (in red) again. Solid vertical lines are used to indicate the time corresponding to each snapshot at the left. The snapshot of Model

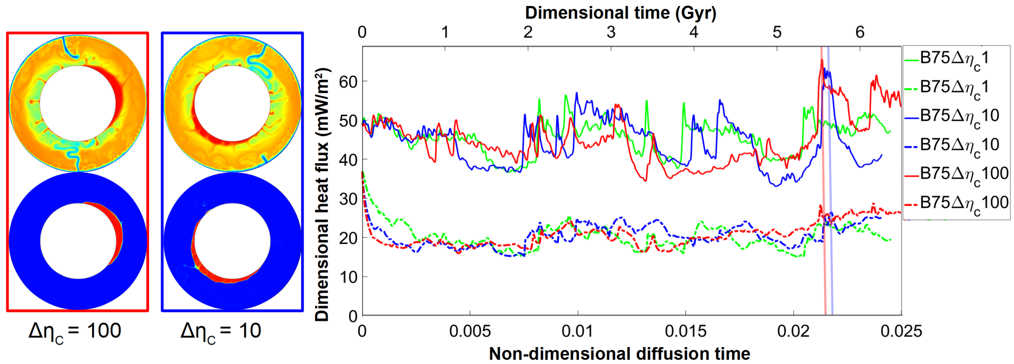

Figure 3. (Thermal and compositional field snapshots from Models 2DB0.75D100 (left) and 2DB0.75D10 (right) and the corresponding CMB (dashed) and surface (solid) mean heat flux time series. Heat flux is shown in dimensional units of $\mathrm{mW/m^2}$ by using the values from Table 1, while dimensional time is provided on the top x-axis and non-dimensional (diffusion) time is given on the bottom axis. The times corresponding to each snapshot are indicated on the heat flux plots by a vertical line of the same colour as the associated heat flux curves.

2DB0.75D100 features a high surface heat flux and two downwellings, while the snapshot from Model 2DB1.0D100 corresponds to a period of low heat flux and the existence of only a single region of subduction. In comparison to Model 2DB0.75D100, Model 2DB1.0D100 exhibits significantly lower minimum surface heat flux values during its evolution. These are associated with the intermittent cessation of surface convergence, and therefore downwellings, and the replacement of a continually mobile surface with an episodic regime of convection. Correspondingly, this case features the highest average internal temperatures of all of the 2D calculations presented. Thus we find that in a 2D system, a combined high buoyancy number and intrinsic viscosity contrast can lead to a disruption of the large scale flow owing to intermittent stagnation of the surface.

Figure 5 shows the thermal and compositional field evolution for Models 2DB0.75D100 and 2DB1.0D100. The sequence on the left depicts two distinct piles of anomalously dense material occupying opposite hemispheres throughout the illustrated period. Additionally, the surface of this system features two zones of localized convergence that result in the consistent preservation of widely separated regions of downwelling. The focused subducting material impinges upon the CAID material near the core mantle boundary, forming voids in which no CAID material is present above the CMB. Additionally, as exhibited by the

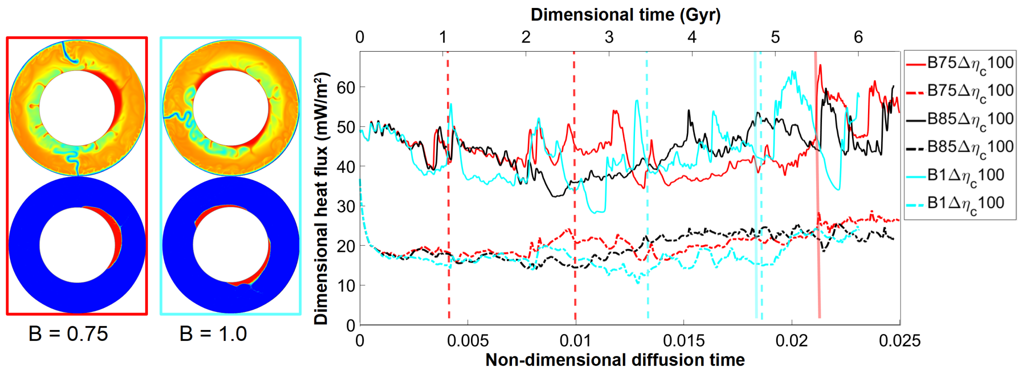

Figure 4. (Thermal and compositional field snapshots for Models 2DB0.75D100 (left) and 2DB1.0D100 (right) and the corresponding CMB (dashed) and surface (solid) mean heat flux time series. Heat flux is plotted in dimensional units of mW/m^2 while dimensional time is provided on the top x-axis and non-dimensional (diffusion) time is shown on the bottom axis. The times corresponding to each snapshot are indicated by a solid vertical line of the same colour as the associated heat flux curve. Dashed vertical lines bound the time ranges presented in Figure 5.

northern hemisphere evolution between 0.95 and 1.58 Gyr, downwelling lithosphere can act to further shape CAID material into narrower piles with steeper sides. Moreover, the height of the piles in the two hemispheres can differ by roughly a factor of two.

Model 2DB1.0D100 displays a greater transience in the CAID material distribution over a slightly shorter period; initially two diametrically opposed piles are present, which coalesce into a single pile before breaking apart again. Unlike Model 2DB0.75D100, the surface of Model 2DB1.0D100, features only a single region of focused convergence throughout the illustrated period. Accordingly, the system is less efficiently cooled by subduction and is persistently hotter. At time 0 Gyr, downwelling material originating near "two o'clock" sinks to the core mantle boundary driving the CAID material to move laterally about the CMB. At time 0.52 Gyr, the downwelling material has spread over the CMB forcing the CAID material into a single pile covering most of the CMB in the opposite hemisphere. At 0.78 Gyr, downwelling at two o'clock ceases and a new region of downwelling forms above the centre of the CAID province. By 1.04 Gyr, the downwelling has generated a new void in the CAID material coverage of the CMB and has re-established a two pile distribution.

These two cases illustrate the impact of plate convergence on the formation of diametrically opposed provinces. More than one persistent downwelling is required for long term

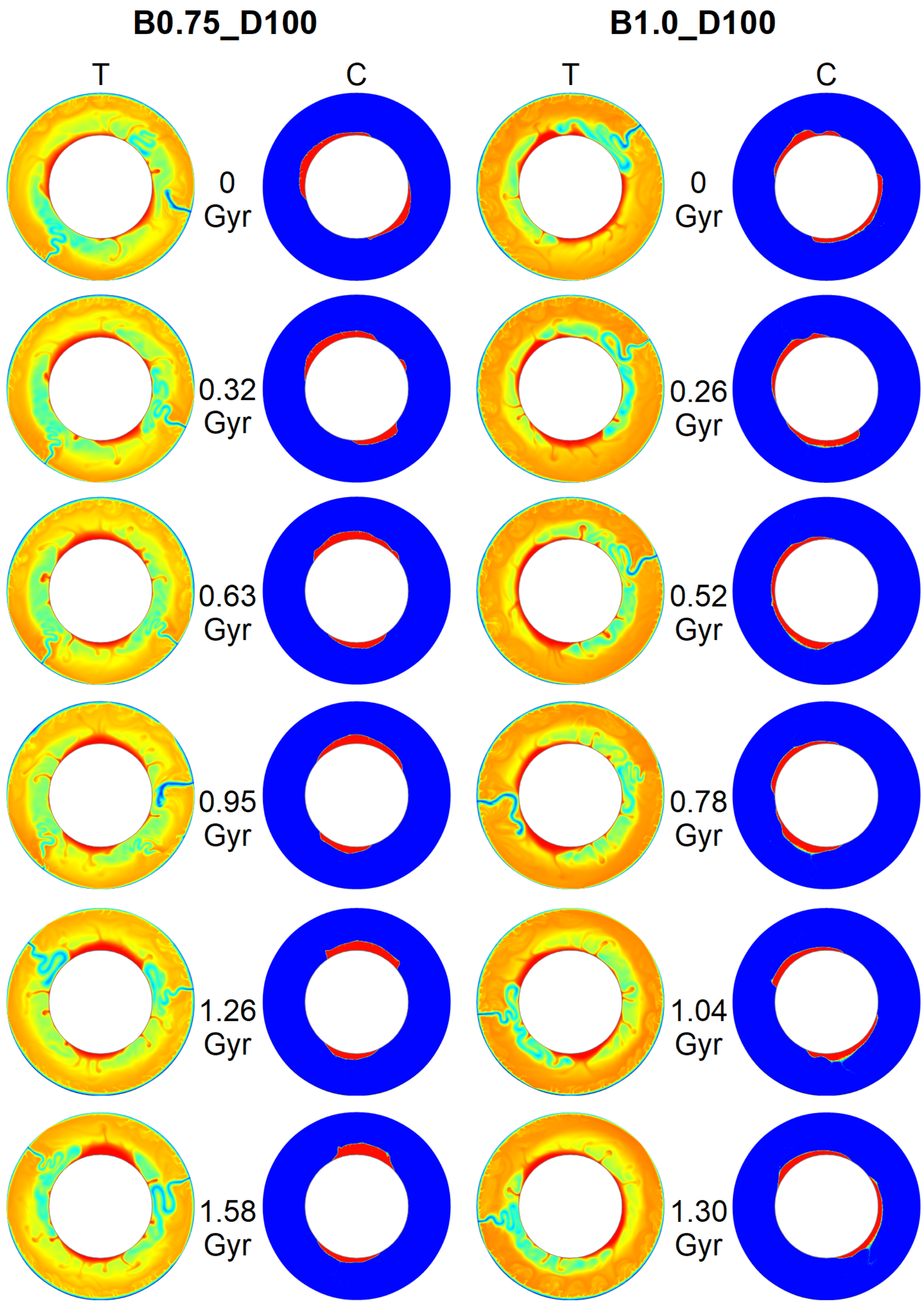

Figure 5. A series of thermal and compositional field snapshots for Models 2DB0.75D100 (left) and 2DB1.0D100 (right) displaying the evolution of each case over approximately 1.5 Gyr. An age is indicated next to each set of annuli images indicating the time that has passed since the top-most panel. The times corresponding to the first and last snapshot are indicated by dashed vertical lines in Figure 4. The temperature scale is the same as in Fig. 1.

maintenance of two diametrically opposed provinces. Subduction initiated over a void in CAID material coverage of the CMB will enforce the coalescing of material into a single pile, while subduction initiated over a province will often divide the province into two piles. If, in the latter case, the subduction is robust and long lasting the piles will once again coalesce into a single province in the opposite hemisphere. Of final note, feedback between the CAID material and plate convergence zones can result in global temperature changes that are conducive to the intermittent cessation of surface mobility.

3.5 Three-dimensional convection calculations

Although we expect some of the behaviour observed in two-dimensional calculations to be maintained in three-dimensional systems (e.g., the impact of the intrinsic viscosity contrast of the two component system as well as the influence of the buoyancy number on province height and total core coverage), the limited degrees of freedom in the two-dimensional system can result in dynamics that will not be reproduced in a full spherical shell; suggesting the potential for some departures from the 2D behaviour. For example, the CAID material piles formed in 2D systems break apart and disperse over the CMB in a similar way to the modelling of supercontinent breakup and dispersal at the surface of the mantle (Gurnis, 1988). However, limitations caused by restricting the migration of distinct components, like continental lithosphere (Zhong & Gurnis, 1991) or CAID material provinces (Langemeyer et al. 2020), to motion on a great circle can force cycles that are unlikely to be realized in three-dimensions, or eliminate realistic alternatives for evolution that require three dimensions. For example, 2D systems can only model supercontinent cycles that replicate end-member paradigms for ocean opening and closure, rather than the spectrum of possibilities that actually exist (Murphy & Nance, 2004, Rolf et al., 2012). Moreover, in two dimensions, changes in the direction of the migration of a dense province requires reversals, as with changes in plate motion (e.g., Lowman et al., 2001). In the case of plate motion this restriction can introduce episodicity (Koglin et al., 2005), including brief periods of stagnation, and therefore an affect on global temperatures.

A 3D model will allow for different options in the location, relative orientation and distribution of downwellings originating along bands of surface convergence. In the remainder of this study, we focus on how the feedback between downwellings and CAID material affects the formation of CAID provinces within a 3D system. Additionally, we analyze the impact of the CAID material component on the evolution of localized regions of deformation at the surface. Specifically, we investigate whether a two component deep mantle affects the mobility of plates and whether the contrasting structure of convergent and divergent surface features is persistent; as observed in the isochemical calculation (Langemeyer et al., 2021) .

In addition to the uniform (2×10^7; 110 MPa) yield stress calculations that allow for a direct comparison with the two dimensional model results, we investigate the impact of a reduction in the surface yield stress on the interior thermal structure and the distribution of CAID material. In this case, the surface yield stress has been weakened by a factor of two but increases linearly until reaching a non-dimensional depth of 0.02 (60 km), below which the yield stress is again set at a constant valued 2×10^7. This alternative model is conducive to generating more convergent bands that result in downwellings (although, for isochemical models, it is much less effective in producing a dichotomy in the structure of divergent and convergent boundaries; marked by the appearance of transform faults in the former case). The choice of investigating cases with a weaker surface is prompted by an understanding that the CAID material is driven into piles by its interaction with downwellings, and that adjusting a primary factor affecting the formation of downwellings may have a profound effect on recovering a system with a pair of distinct provinces and a plate tectonic-like surface.

3.6 Initial condition for the 3D calculations

Figure 6 presents snapshots of the initial conditions used for the 3D calculations. Figure 6a shows viscosity and divergence field snapshots for the initial condition used to start all 3D calculations featuring a uniform yield stress. In addition, the interior thermal structure is displayed utilizing hot and cold isosurfaces corresponding to focussed upwelling and downwelling material, respectively, as well as the corresponding temperature field power spectrum (horizontal) as a function of non-dimensional height (vertical) above the CMB. Similarly, Figure 6b shows the initial condition utilized for all depth-dependent yield stress calculations described. The initial conditions were generated from calculations in which a CAID component is absent. In the uniform yield stress case, the surface features just three plate-like regions at the time shown, however, for the parameters selected, half-a-dozen plates often evolve. Moreover, the parameters are identical to those chosen in the earlier 2D computations and have demonstrated compatibility with the generation of distinct CAID provinces in that geometry. The surface zones of convergence and divergence are distinct in their structure with the former appearing as smooth continuous (arcuate) bands and the latter appearing as a series of spreading centres (analogous to ridges) punctuated by offsets (analogous to transform faults). The depth-dependent yield stress case exhibits an initial condition featuring more distinct plate-like regions but less well defined divergent boundaries (and no transform-like offsets). The surface shows a number of zones of focused deformation and power across a band of harmonics (peaking at degree three). The cases presented in the remainder of this study are initiated from these fields with a uniform thickness layer of CAID material (accounting for 3.0% of the mantle volume) enveloping the CMB, unless noted otherwise.

3.7 CAID material distribution in three-dimensional calculations

Figure 7 presents snapshots from nine calculations incorporating intrinsically dense material with different buoyancy numbers and viscosity contrast owing to composition. These cases all feature a uniform non-dimensional yield-stress of $2{\times}10^7$. In addition to the viscosity field just below the surface, a hot interior isosurface and the CAID material distribution are shown. The rendering of the surface viscosity field utilizes the same colour definitions as the images presented in Figure 6, while the red and blue isosurfaces show a thermal cut-off of non-dimensional temperature 0.82 and the distribution of CAID material, respectively. For the same cases, images from temporally corresponding but diametrically opposed viewing angles are presented in Supplementary Figure 1. For a number of cases, following the introduction and evolution of the CAID material, similar divergent and convergent surface features to those exhibited in the isochemical initial condition are maintained. In addition, the length-scale of these plate boundaries is maintained in many cases, with long bands of deformation persisting for a mantle transit time or longer, such as in Models 3DB1.0D10 and 3DB0.85D100 which exhibit focussed weak zone bands subtending 180°. Some snapshots, such as for Model 3DB1.0D1, display a surface with a greater number of weak zones (as revealed by the near surface power spectrum) resulting in an increased number of isolated surface regions analogous to distinct plates. However, in all cases, far fewer plate-like regions are found than is currently observed on Earth.

A variety of CAID material distributions are shown in Figure 7, however, despite frequent sampling, none of the cases examined with this yield stress model were found to produce a persisting pair of CAID material provinces, as would be analogous to the structure of the LLSVPs observed at the base of Earth's mantle. Supplementary Figure 2

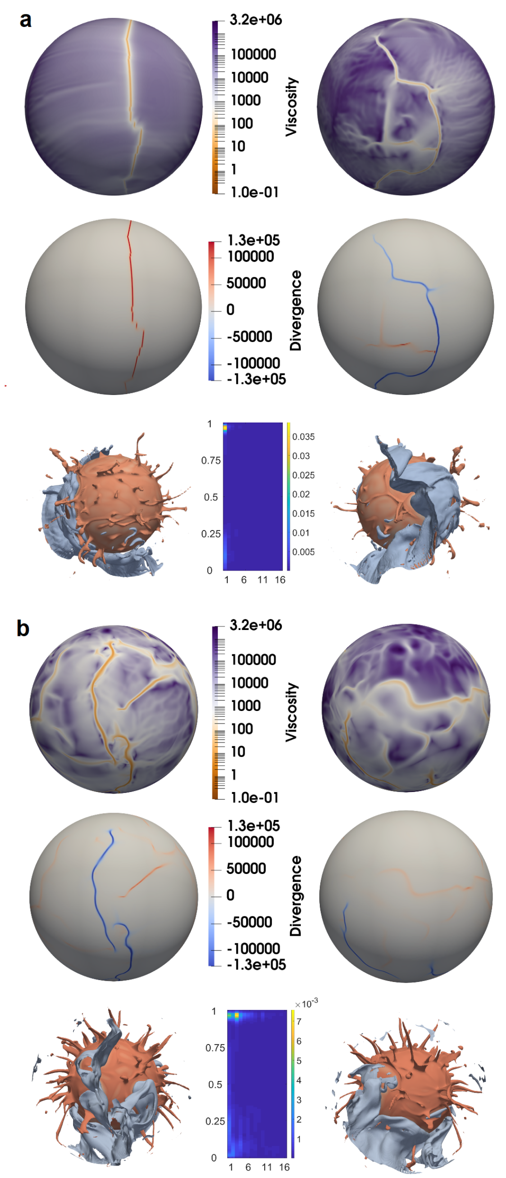

Figure 6. The initial conditions used for the initiation of uniform yield stress (2×10^7; 110 MPa) 3D calculations (a) and cases with a depth-dependent yield stress (surface $= 1 \times 10^7$, interior $= 2 \times 10^7$) (b). Near surface viscosity and non-dimensional divergence as well as internal thermal structure and its power spectra (as a function of height above the CMB) are presented for each case. The thermal isosurfaces correspond to non-dimensional temperatures of 0.82 (red) and 0.42 (blue). The left and right columns show diametrically opposed views. Cold isosurfaces are clipped at a non-dimensional depth of 0.05 to reveal the thermal interior structure. All 3D model calculations are carried out in a spherical geometry utilizing a yin-yang grid with a resolution of $96 \times (768 \times 256) \times 2$ and 930 million tracers.

presents Mollweide projections of the compositional field 145 km above the CMB in nine plots corresponding to the snapshots shown in Fig. 7. The most common distribution of CAID material observed is that of a single large pile, typically extending over an area of at least one hemisphere. Generally, large voids are carved out of the dense layer by robust downwellings sinking to the core mantle boundary. Some smaller piles of CAID material are seen in Model 3DB1.0D100 of Figure 7 and Model 3DB0.85D10 of Supplementary Figure 1. Only a small amount of the total CAID component is included in these isolated piles and typically they tend not to be completely detached, but rather are connected to the larger piles by tendrils of the CAID component reaching across the CMB. As was found in the study of the 2D cases, the height and steepness of the piles appears to be greatest when the intrinsic viscosity of the dense component is large relative to the ambient mantle. Those cases where $\Delta\eta_C$ equals 100 feature the greatest altitude and steepest sided piles. In accord, these cases can also exhibit less core coverage by the CAID component. A low buoyancy number CAID component is less resistant to being forced aside by cold downwelling material. Consequently downwellings can push a lower buoyancy ratio dense component laterally as the reduced density of the piles means they are more readily deformable as well as able to rise to higher altitudes. Furthermore, CAID material with an increased $\Delta\eta_C$ will respond more slowly to the opportunity to spread around the core mantle boundary during periods when the pile experiences diminished lateral forcing.

3.7.1 Temperature field power spectra

For each case in Fig. 7 a plot of the thermal power spectra as a function of height above the CMB is shown in Supplementary Figure 3. The power spectra indicate the dominant degrees in the upper thermal boundary layer as well as the distribution of the CAID material in the deep mantle. Long wavelength peaks in the power spectra near the surface of the systems are typical, with the greatest power usually occurring at degree one or two, corresponding to the number and spacing of bands of focussed surface deformation. In addition to the strong degree one or two surface power observed, a subset of cases including Models 3DB1.0D1 and 3DB0.85D100 display some power in higher degrees. In particular, these cases feature a greater number of bands of lithospheric weakness traversing shorter distances across the surface. The power focused in the lowest degrees in the mantle, just above the CMB, results from the influence of CAID material distribution and is generally much stronger than focusing observed at the surface. Due to the relatively low buoyancy of

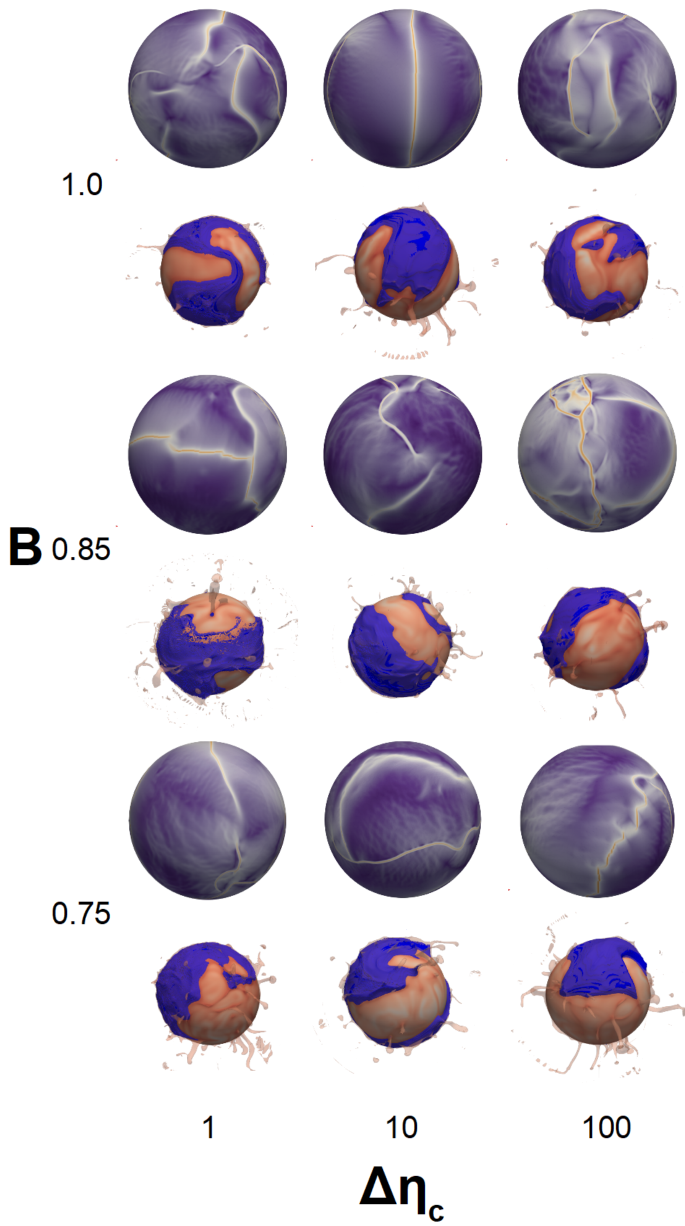

Figure 7. Snapshots from the nine uniform yield stress 3D cases featured in this study. The buoyancy number and intrinsic viscosity contrast for the CAID material and ambient mantle are indicated at the left and bottom of the figure, respectively. For each case, the viscosity field is shown at a depth of $0.005d$ juxtaposed with a (to scale) image of the mantle interior illustrating CAID material distribution (in blue) and thermal plumes (transparent red, non-dimensional temperature of 0.82). (The viewing angle of the viscosity field and model interior are the same.) The temperature power spectra corresponding to each snapshot is presented in Supplementary Fig. 3.

the CAID material, a large amount of heat is trapped in the dense provinces so that thermal power spectra indicate the nature of the intrinsically dense material's distribution. As with the power spectra at the surface, predominantly degree-one to -two power is observed, indicating that the CAID material is typically grouped into a single large pile but that a capacity for distribution into two piles exists. Cases featuring a buoyancy number of 1.0 display power in harmonics as high as degree 3 (and 4), most likely because those cases exhibit a higher occurrence of shorter, localized, near-surface, deformation zones that (2D results indicated) are capable of promoting small isolated piles (e.g., Model 3DB1.0D100) or simply more discontinuity of the CAID layer. We note that the locations associated with surface weakening are not clearly imprinted on the underlying CMB by an absence of CAID material. This suggests that the migration of lithospheric weak zones may be at least as fast as the rate of arrival of sinking material at the CMB. However, as in the two-dimensional systems analyzed, we find that the arrival of downwellings at the CMB pushes aside CAID material so that its distribution is largely influenced by plate convergence. The results of the three-dimensional cases indicate that an apparent influence of the feedback between the plate boundary distribution and CAID material placement is the similar focus in low degree powers. Model 3DB1.0D10 is one of the two cases shown that features its strongest power at the surface in the degree two signature. It is examined in detail in section 3.7.3.

3.7.2 Transience in the heat flux

Figure 8 displays heat flux time series for the three cases appearing in Figure 7 featuring a buoyancy number of 0.75. We find no clear impact on the trend of the CMB heat flux values or their temporal variation for the range of intrinsic compositionally originating viscosity contrasts examined. As in the 2D calculations employing the same parameters (Figure 3), the surface heat flux is highly time-dependent, however, it shows less variation in the 3D calculations (e.g., when comparing the ratios of maximum to minimum value). In the two-dimensional cases, roughly 100% increases in surface heat flux are possible while the largest swing in heat flux in the 3D cases is closer to 50%. Consistent with the 2D results of Figure 3 we observe that spikes in heat flux are associated with the initiation of new downwellings. The 3D downwellings are structurally more complicated than the 2D downwellings but a greater degree of freedom is present in fully spherical environments. Thus, smoother and less dramatic variations in amplitude occur between periods of low heat flux and high heat flux because surface velocities do not need to slow when plates change direction. For example,

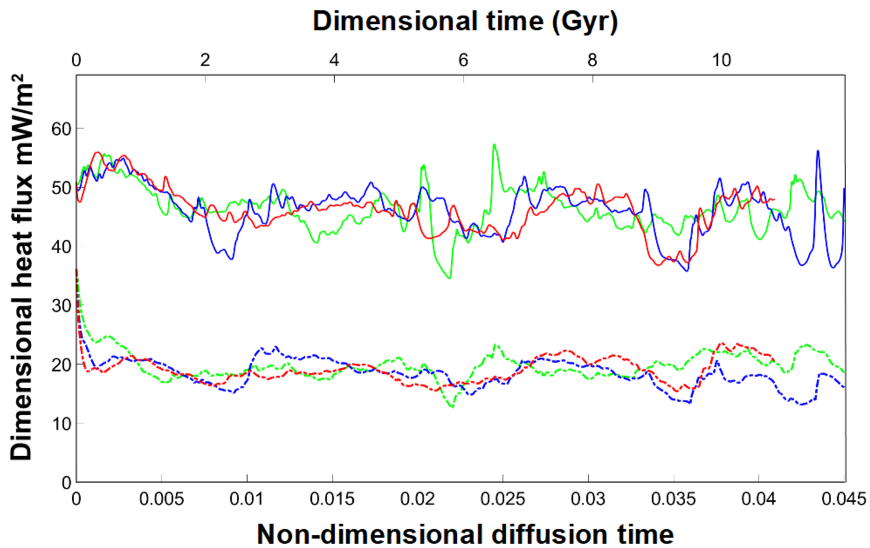

Figure 8. Surface and basal heat flux time series for the three 3D cases with uniform yield stress featuring a buoyancy number of 0.75. Green, blue and red correspond to cases where $\Delta\eta_C$ equals 1, 10 and 100, respectively. The time series illustrate surface and basal heat flux values using solid and dashed lines, respectively.

in a 2D model, if one convergent boundary closes while another emerges, plate directions can reverse and velocity briefly drops to zero. However, in 3D, changes in plate direction do not require a reduction in the global surface velocity and the initiation of new subduction zones is less impactful on surface heat flux. A notable difference between the 2D and 3D calculations is that the variation in heat flux was reduced when $\Delta\eta_C = 1$ in 2D cases, which was attributed to the prevailing degree-2 flow in this case, versus a degree-1 trend in the other cases. In the 3D cases, we do not observe such a trend in heat flux or a clear contrast in the power spectra harmonics, we attribute this to the added degree of freedom of the 3D systems that removes the discretized contrast between degree-1 and degree-2 flow. One similarity between the two-dimensional and three-dimensional models is that increases in surface heat flux typically correspond to an increase in heat flux at the CMB.

Figure 9 presents heat flux time series for the three cases shown in Figure 7 featuring $\Delta\eta_C$=100 (n.b., Model 3DB0.75D100 (red) appears in both figures). In contrast to the three cases in Figure 8 with a common buoyancy number, these heat flux profiles show a trend.

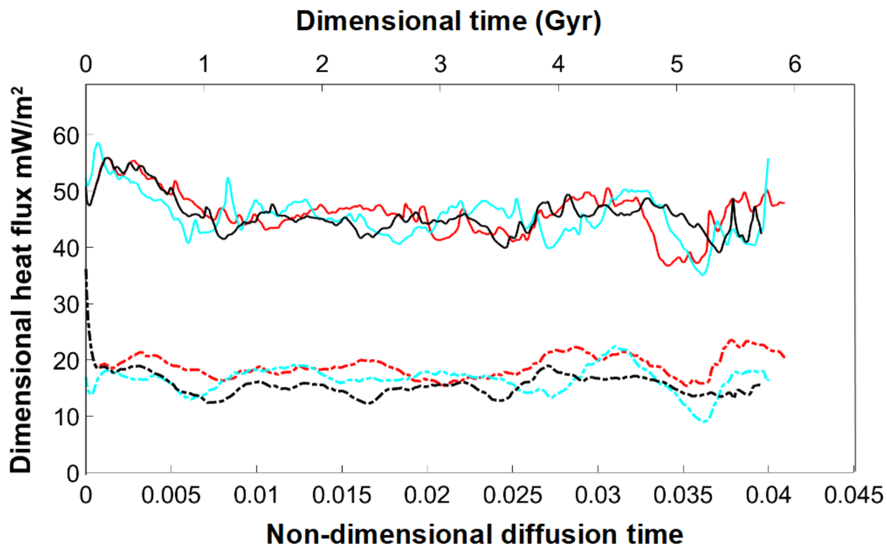

Figure 9. Surface and basal heat flux time series for the three 3D cases with uniform yield stress, featuring CAID material with an intrinsic viscosity that is 100 times greater than the ambient mantle. Red, cyan and black correspond to cases where B = 0.75, 0.85 and 1.0, respectively. The time series illustrate surface and basal heat flux values using solid and dashed lines, respectively.

The heat flux diminishes as the buoyancy ratio is increased (this can be seen most clearly in the basal heat flux times series). Furthermore, for a corresponding CAID material viscosity the buoyancy number 0.75 cases are hotter in 3D calculations. The transience of surface and basal heat flux is again observed but the transition from periods of low heat flux to high heat flux occurs over longer periods and the range of minimum and maximum heat flux values is narrower than in the analogous 2D cases. The basal heat flux trend agrees with the findings of the 2D calculations which demonstrated that an increased buoyancy number can result in greater insulation of the CMB.

3.7.3 Evolution of the plate boundaries and CAID material distribution

We now examine the detailed time-dependence of one of the cases from Figure 7. The time-averaged power spectrum for the temperature field of Model 3DB0.75D10 showed a peak in lower mantle power at degree 2. A period of 1 Gyr of evolution (ending at the time shown in Figure 7) is analyzed here in order to determine whether this spectral peak ever corresponds to two distinct provinces.

Figure 10 displays six sequential snapshots of the near surface viscosity field as well as isosurfaces that reveal plumes (red, non-dimensional temperature of 0.82) and CAID material distribution (blue) for Model 3DB0.75D10. Each row shows an instant in time as viewed from diametrically opposed positions. Additional viewing angles are presented in Supplementary Figure 4. The viscosity field shows the evolution of features such as narrow weak bands (corresponding to convergence and divergence) that bound the low strain-rate plate-like regions. In addition, at times 200 Myr and 400 Myr the viscosity fields display the formation, evolution and dissolution of transform-like offsets along spreading boundaries. The feedback between surface features and the distribution of the CAID material is illustrated in the column marked 0° in Fig. 10 , from times 600 Myr to 1 Gyr. The snapshot at time 600 Myr features CAID material that forms a great province extending from the northern to southern pole. At time 800 Myr the previously discontinuous convergent bands in the left and right hemispheres (roughly coincident with the equatorial region in the figure) have merged, forming a triple junction with a spreading boundary located in the southern hemisphere. The merging of the convergent boundaries has lead to the development of a sheet-like downwelling that plunges into the deep mantle and impacts the CAID material below, pushing aside the dense material. Accordingly, the north-to-south pole extending province becomes split into a north and south fragment. In general, large voids are present in the CAID material below convergent surface features. Conversely, spreading boundaries incorporating transform offsets are most typically found over regions of the CMB covered by CAID material. This characteristic mimics the behaviour observed in the two-dimensional cases.

We note that in this calculation, the movement and repositioning of the CAID material's periphery on the CMB occurs on the same time scale as the motion of the plate boundaries. Accordingly, plumes anchored at the peripheries of the CAID provinces migrate at similar rates. Some plumes form on top of the CAID material piles, below divergent surface features, but they lack the vigour needed to penetrate into the upper mantle.

In Supplementary Figure 5 we present Mollweide projections of the compositional field 145 km above the CMB for each of the times corresponding to Fig. 10. Given the full 360° view of the CAID material shown in Supplementary Fig. 5 a brief period of two province formation is revealed at 0 Myr. However, unlike Earth's LLSVPs, the separation of the provinces is relatively small. Moreover, it does not persist. This period marks the only time we observe the formation of two provinces. The distribution of the CAID material in this epoch apparently produced the degree-2 signature in the time averaged power spectrum of the model's thermal field.

Given the evidence that downwellings drive the formation of regions on the CMB that are void of CAID material, we explored the dependence of the distribution of the CAID material on downwellings by reducing the surface yield stress to allow for a greater number of convergent bands in the model lithosphere. Model 3DB0.75D100weak is similar to Model 3DB0.75D100 except that it employs the weaker yield stress model described in section 3.6 and initializes by placing a CAID layer in the thermal field shown in Fig. 6b. The yield stress increases with depth over the top 2% of the mantle from a non-dimensional surface value of 1×10^7 to a uniform yield stress of 2×10^7 at all lower depths.

Figure 11 presents a series of snapshots for Model 3DB0.75D100weak. The viscosity field snapshots exhibit the increased number of convergent and divergent surface bands resulting from the weakening of surface yield stress, leading to the development of a greater number of downwellings and individual plates. (However, with the weakened surface the calculation no longer exhibits the transform-like offsets punctuating divergent features.) The increased number of smaller scale downwellings leads to a greater number of voids within the layer of CAID material. For example, multiple voids are observed in the column marked 0° at time 540 Myr in Fig. 11; column B at time 900 Myr of Supplementary Figure 6; and column D times 360 to 720 Myr (also Supplementary Figure 6); varying in size and number. Accordingly, the CAID material tends to form a greater number of narrow tendril-like features joining the piles on the CMB, as exhibited in the columns marked 0° of Fig. 11 and 90° (B) in Supplementary Figure 6.

Supplementary Figure 7 shows the compositional field 145 km above the CMB at the times presented in Figure 11 and illustrates the growth and movement of voids in the dense layer rather than coalescing of the dense material into piles. The formation of numerous connecting branches between larger nodes occasionally allows for the isolation of a fraction of the CAID material into small, short-lived piles. This is exhibited in the 0° column at times 540 to 900 Myr, where a small pile is loosely connected to the greater mass of CAID material by narrow tendrils, briefly isolated (e.g., at 720 Myr in Supplementary Figure 7)

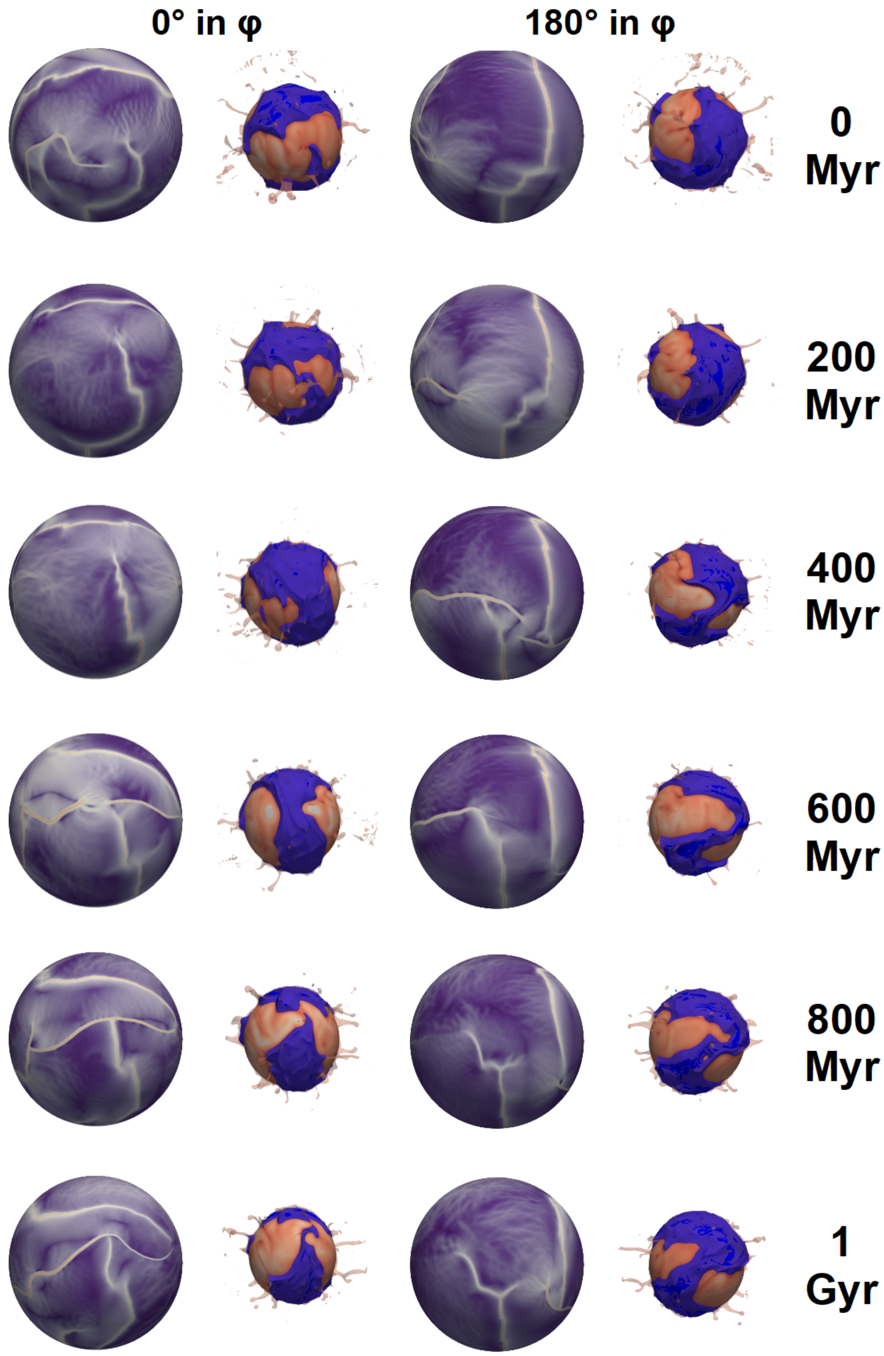

Figure 10. Snapshots of the near surface viscosity field and CAID material distribution at six different times (rows) throughout the evolution of Model 3DB0.75D10. Diametrically opposed viewing angles are presented for each time, with the angle of rotation relative to a vertical axis through the centre of the sphere in the left-most column indicated at the top of the second column. Additional viewing angles are presented in Supplementary Figure 6.

and then rejoined to the larger pile through another narrow tendril. The weakening of the surface yield stress thus leads to the formation of a greater number of small scale features at the surface (including downwellings) and a CAID distribution on the CMB that might be described as 'fragments connected to a large province incorporating voids'. However, aggregation into two similar volume provinces is not obtained during the more than 1 Gyr modelled.

Figure 12 shows thermal power spectra as a function of height above the CMB for the model presented in Figure 11. Although the distribution of the CAID material during this period appears unchanged from a qualitative perspective, the thermal power spectra indicate a field dominated by degree-2 above the CMB has transitioned to a field with a degree-1 signature, in addition to lesser power distributed as high as degree-6. Given their hot signatures we infer that periods dominated by degree-2 CAID material distribution occur, but detection of such a period is not an indicator of a pair of detached provinces.

To explore the possibility that the critical issue inhibiting the formation of two distinct provinces in our calculations is the specification of an excessive volume of the CAID material, we examined a final case incorporating a reduction in the volume of the intrinsically dense component. Model 3DB0.75D100weak&reduced employs identical parameters and initial condition to Model 3DB0.75D100weak but the CAID component incorporated in the calculation comprises only 2% of the mantle volume. Figure 13 shows the evolution of Model 3DB0.75D100weak&reduced by presenting the divergence field and temperature field power spectra as a function of height above the CMB. The corresponding evolution of the near surface viscosity field and thermal power spectra is presented in Supplementary Figure 9. The corresponding evolution of the dense layer is shown in Supplementary Figure 10. As in the other calculations presented, at time 0.0 Myr the mean temperature of the model has equilibrated following the incorporation of the CAID layer into the initial condition thermal field (Fig. 6b) and subsequent forward modelling. Although the reduction in the volume of the CAID component does not result in a pair of distinct provinces during the evolution of this case, the introduction of the denser material does have a global impact on temperature that results in the formation of a greater number of distinct plates and triple junctions than in either the isochemical initial condition models or the previously described case (Model 3DB0.75D100weak) featuring a higher volume of CAID material. Moreover, the divergent boundaries exhibit multiple examples of transform-like offsets (e.g., the boundary extending 'north-south' in the column marked 180°). The influence of a CAID mantle component on

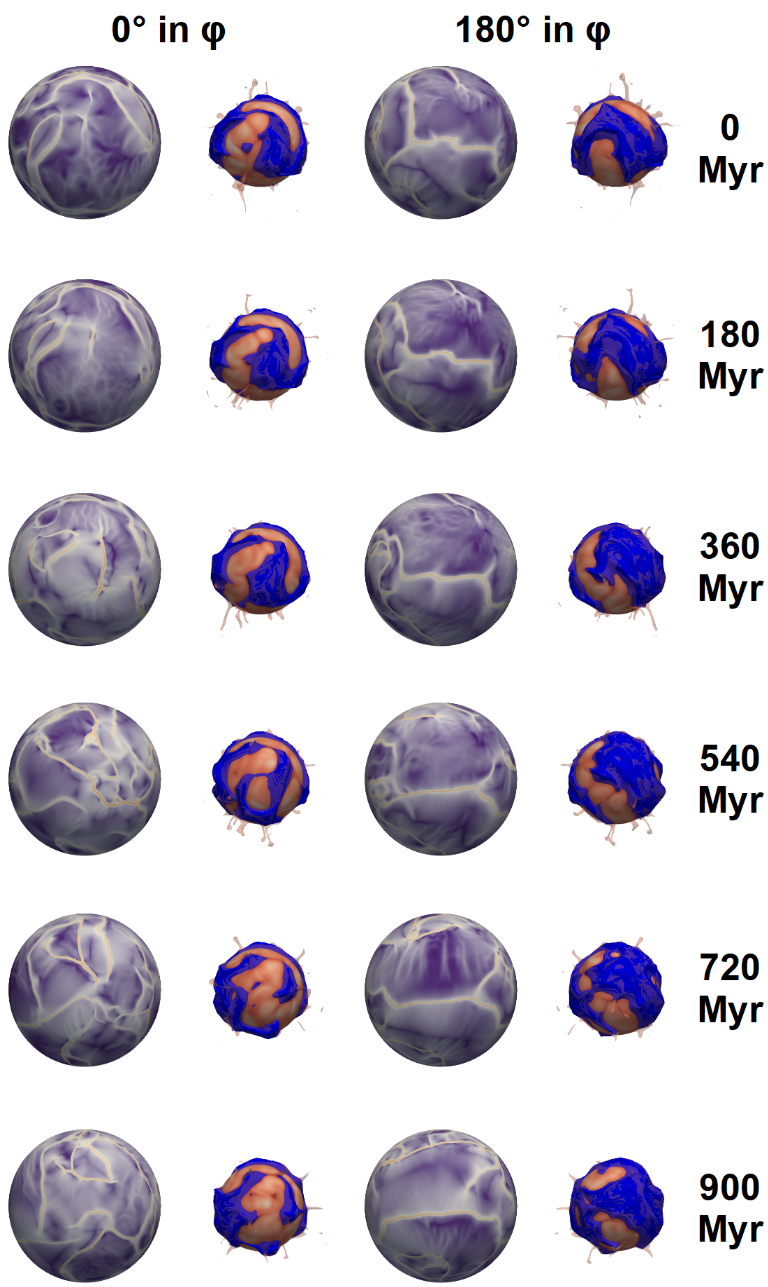

Figure 11. Snapshots of the near surface viscosity field and CAID material distribution at six different times (rows) throughout the evolution of Model 3DB0.75D100weak. Diametrically opposed viewing angles are shown for each time with the angle of rotation relative to the left-most column indicated at the top of the columns. Supplementary Figure 6 presents additional viewing angles of the viscosity field and CAID material distribution at the same times.

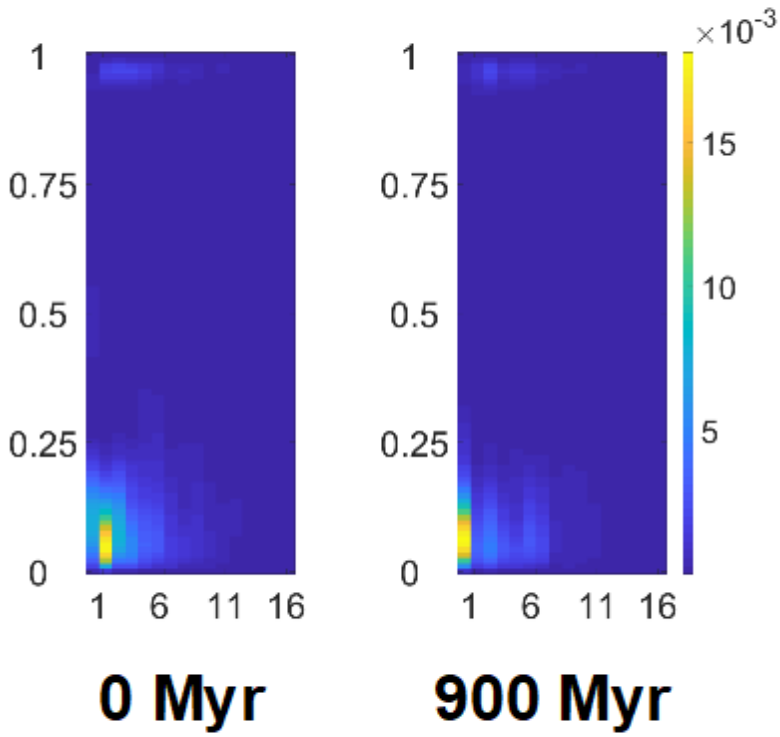

Figure 12. Thermal field power spectra as a function of height above the CMB for the case presented in the previous figure. The timing of the spectra presented corresponds to the first and final frames shown above.

the formation of plates is illustrated by the impact of plates and dense provinces on the temperature field of the systems examined.

Figure 14a depicts temperature profiles taken from the initial condition models in Fig. 6 (red and cyan curves) as well as time-averaged profiles from the cases presented in Figs. 10, 11 and 13 (magenta, green and blue, respectively) and shows the impact on global temperature of both a weakened lithospheric yield stress and the presence of a hot CAID component sitting on the CMB; specifically the insulation of the mantle from core heat flow that emplacement of this component engenders. The influence of a lower lithospheric yield stress is revealed by comparing the red and cyan curves, which show the substantial cooling resulting from a greater number of downwelling sheets that form with a lowered yield stress. With the addition of the CAID material, temperature increases in the lowest 15-20% of the mantle relative to the isochemical cases. The increased temperature extends to a smaller height above the CMB in the case where the volume of the intrinsically dense material is reduced (blue curve). In all cases featuring a CAID component, the mantle above the deep layer incorporating the CAID component is cooler than in the corresponding isochemical case because the denser material sitting on the core reduces heat flow into the mantle. The degree of mid-mantle cooling is clearly determined by the volume of the CAID material. This is illustrated by comparing the green and blue curves: the lower volume of CAID material in Model 3DB0.75D100weak&reduced (blue) results in a warmer mantle in that case, relative to that of Model 3DB0.75D100weak (green), above the depths that incorporate the CAID material. (At the same time, the blue curve is cooler than the magenta because the model producing the latter has a weaker surface and allows for a longer network of interior-cooling (convergent) plate boundaries.) However, the blue curve (2% CAID material) is hotter than the cyan (no CAID material) in the upper mantle and the cyan curve is just mildly warmer than the green (3% CAID material). This departure from the other systematic trends is a manifestation of what is effectively a regime change in the lithospheric character. The cyan curve (the initial condition model with a weaker lithospheric yield stress) corresponds to a case with a mobile surface but less distinct plates and boundaries than in the uniform yield stress cases. Adding the 2% CAID component to the mantle has affected global flow so that a cooler mid-mantle and hotter upper mantle evolves. The result is conducive to producing more clearly defined plates isolated by tightly focussed boundaries.

Figure 14b shows the viscosity profiles corresponding to the temperature profiles in 14a, emphasizing that the heat trapped in the CAID material counteracts the high intrinsic

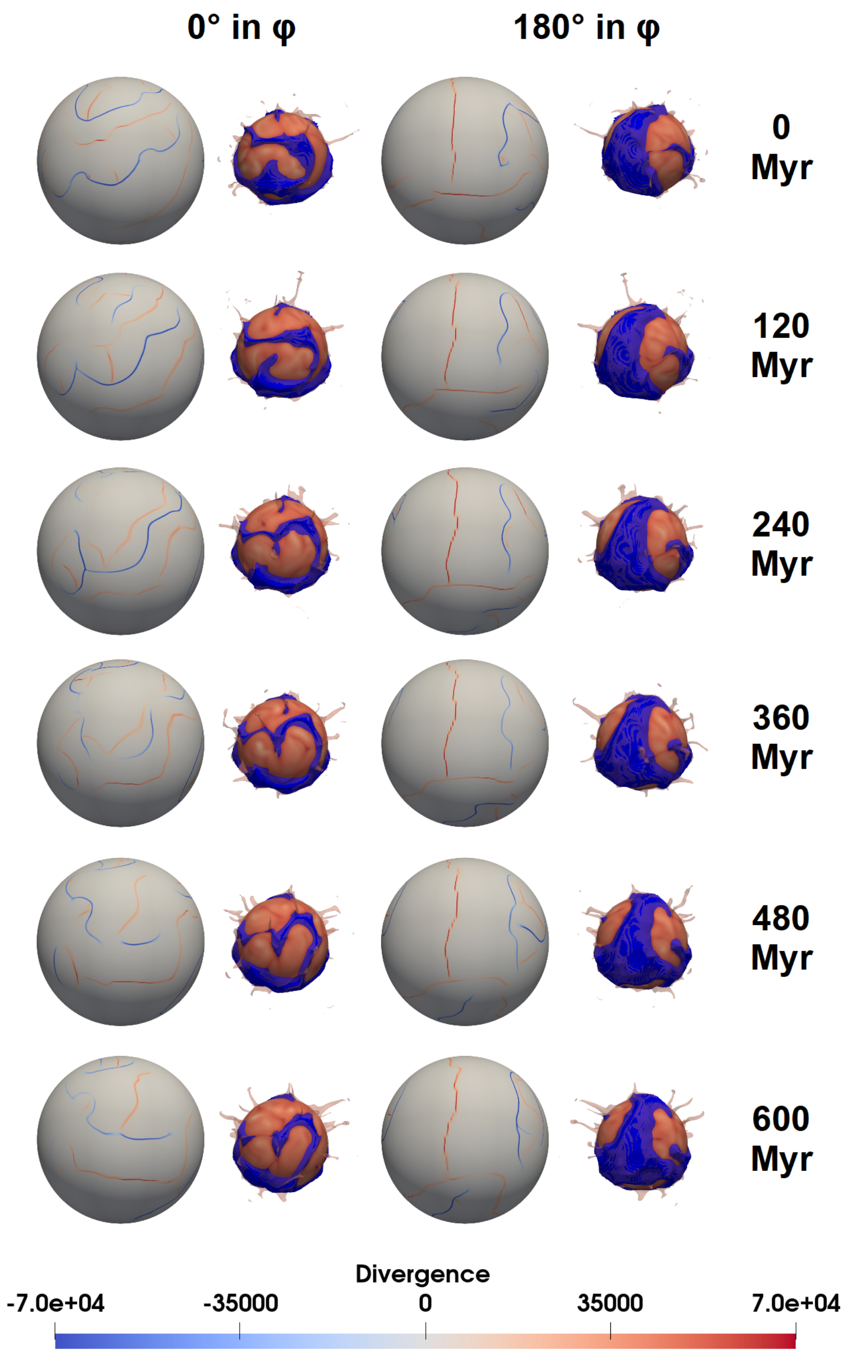

Figure 13. Snapshots of the near surface non-dimensional velocity divergence field and CAID material distribution at six different times (rows) throughout the evolution of Model 3DB0.75D100weak&reduced. Diametrically opposed viewing angles are shown for each time with the angle of rotation relative to the left most column indicated at the top of each column. Additional viewing angles are shown in Supplementary Figure 8.

viscosity of the dense components to such a degree that the isochemical cases exhibit the highest mean viscosity in the region between the deepest five and fifteen percent of the mantle. The viscosity profiles also show the impact of robust deep penetrating slabs. For example, although hotter at mid-mantle than Model 3DB0.75D100weak, the viscosity profile from the initial condition case with a depth-dependent yield stress shows a higher averaged viscosity. The high mean viscosity is explained by the incorporation of numerous very high viscosity downwellings into the averaging. The exponential law for the viscosity has a large impact on averaging where slabs are present while slabs have a relatively smaller impact on mean temperature at a given height. This effect also produces small scale gradient variation in the viscosity profiles relative to the smoother temperature profiles, particularly in the isochemical (initial condition) cases.

Previous authors (e.g., Stein et al., 2004; Stein & Hansen, 2008; Höink et al., 2012; Lenardic et al., 2019) have described the critical role of mid-mantle temperatures and viscosity increase with depth on the generation and sustained mobility of plates. The findings presented here illustrate that the presence of a compositionally anomalous and intrinsically dense mantle component can impact the mid-mantle temperature profile in a way that influences the global viscosity profile and therefore plate formation and mobility. Finally, lowered lithospheric yield stress and a greater volume of CAID material cool the mantle overall. However, as described above, the intrinsically dense mantle component becomes particularly hot. The combined affects of its temperature and intrinsic density result in a much more marginal increase in the density of the CAID component than is implied by the buoyancy numbers. We discuss this further below.

4 Discussion

Although the origin and physical characteristics of the LLSVPs are contentious, with the exception of secondary details there is broad agreement on the physical bounds and seismic properties of the regions of the mantle that define the locations of the provinces (e.g., Cottaar & Lekic, 2016). Specifically, whatever the cause of the seismic signature, the vast majority of the volume of the mantle satisfying classification as LLSVP is divided into a pair of detached features. The distribution of a chemically distinct volume of the mantle into two distinct features blanketing approximately 30 percent of the CMB while rising over 1000 km above the CMB (Garnero et al., 2016) provides key constraints on efforts to determine the physical properties of the compositionally anomalous material assumed

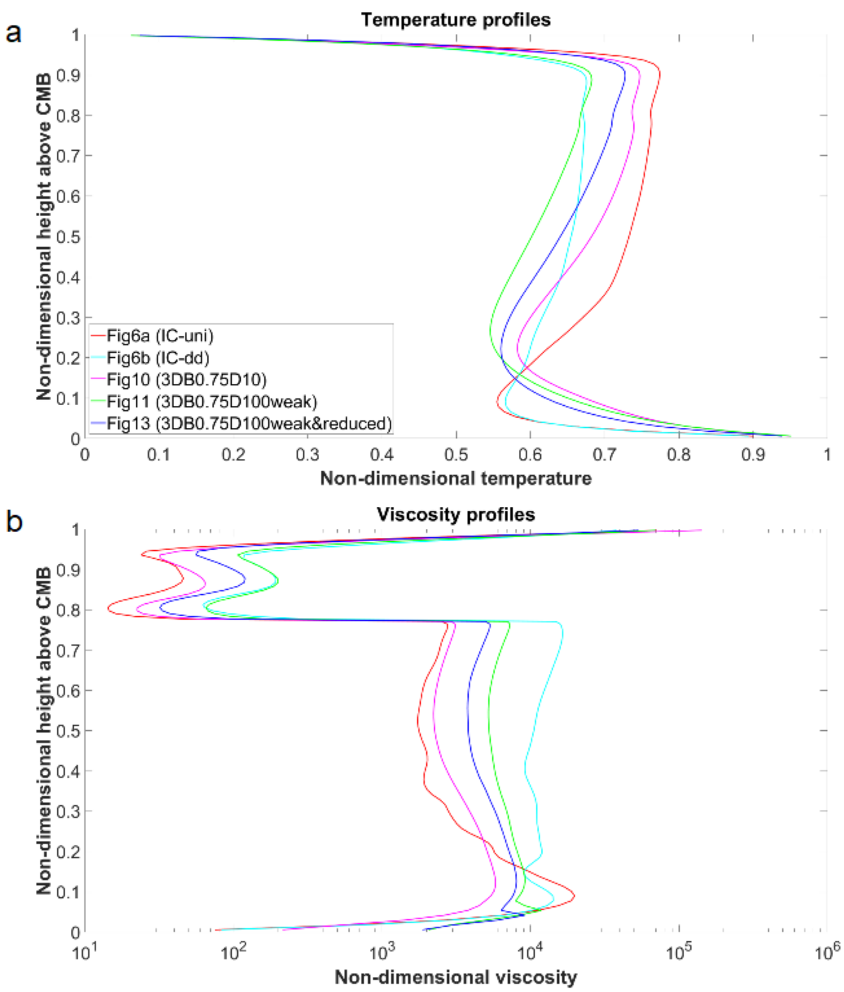

Figure 14. Temporally averaged profiles of the latitudinally and longitudinally averaged temperature (a) and viscosity (b) as a function of height above the core mantle boundary in five of the 3D geometry cases featured in this study. The red curve corresponds to the isochemical initial condition model with a uniform yield stress; the cyan curve corresponds to the isochemical case with the depth-dependent yield stress; the magenta, green and blue curves correspond to Models 3DB0.75D10, 3DB0.75D100weak and 3DB0.75D100weak&reduced, respectively.

responsible for the observation of LLSVPs. Obtaining two detached provinces comprised of such material is not a default distribution of the inclusion of such a component in a 3D spherical shell. In contrast, recovering a pair of large provinces is not as an elusive outcome in two-dimensional models, including the spherical annuli modelled in the first part of this study. We suggest that the challenge of identifying the physical properties of the CAID material that yields LLSVP-type distributions in 3D shells is somewhat analogous to identifying the properties of a fluid mantle that yield sheet-like downwellings. (Two-dimensional calculations with mobile surfaces always produce this desired behaviour, but obtaining slab-like downwelling morphology in 3D spheres is limited to a set of systems with very specific material parameters, initial conditions and shell thicknesses.)

A deficiency of the 3D models that is mostly likely explained by the absence of discrete CAID provinces and a core largely free of coverage by the dense component, is the scarcity of vigorous plumes, capable of transiting the entire depth of the mantle. Given the inferred association of plume generated igneous provinces with chemically originating LLSVPs (Torsvik et al., 2006; Burke et al., 2008; Li & Zhong, 2017; Heyn et al., 2020), the relatively small number of plumes is counter to the expectation of observing PGZs. However, this result is consistent with the observed broad coverage of the CMB by CAID material. Plume generation zones have been inferred to form at the boundaries of relatively small footprint provinces, where thermal gradients can generate plumes. Adjacent to the provinces are broad expanses of the CMB where high heat flow can be drawn into the mantle and advected towards province boundaries. In the 3D cases presented here, the CAID material forms expansive punctured layers with voids that may be too small to draw enough heat from the CMB to allow the formation of robust plumes. In contrast, Langemeyer et al. (2021) found examples of several vigorous plumes transiting the mantle in an isochemical model employing the same parameter values as the 110 MPa uniform yield stress cases presented here. The generally reduced heat flux (and therefore support for plumes) at the CMB, found when CAID material is added to the calculations, is illustrated in Figs. 8 and 9. The contribution to surface heat flow from the core, indicated by the time series in these figures, is in the 10-15% range. This is at the lowest end of widely accepted estimates of CMB heat flow (e.g., Lay et al., 2008). Figure 14 shows that a strong sub-adiabatic temperature profile exists in several models due to slabs pooling in the deep mantle. A sub-adiabatic temperature profile will also decrease the temperature anomaly that characterizes rising plumes.

Overall, our findings do agree with previous studies. By assuming that the origin of the LLSVPs is explained by a chemically distinct lower mantle component, we conclude that the buoyancy ratio of this material (relative to the ambient mantle) as well as an inherent viscosity contrast between the intrinsically dense component and remaining mantle material, both impact the distribution, durability and mobility of the CAID component. For example, when all other system parameters are held constant, increasing the intrinsic viscosity of the denser mantle component tends to result in degree-1 flow, in contrast to the degree-2 structure more readily obtained in the isochemical or chemically enriched cases where $\Delta\eta_C = 1$.

We have excluded the influence of compressibility in our calculations but do not expect this omission to impact the overall dynamics of the systems described given the scale height of the mantle (of order 10^7m.). Nevertheless, compressibility is responsible for decreasing thermal expansivity in the lower mantle. Accordingly, in estimating the total density anomalies occurring in the CAID provinces in these calculations, due to both chemical and thermal affects, an adjustment of the mean thermal expansion coefficient value given in Table 1 is necessary.

For the range of buoyancy numbers considered (0.75, 0.85 and 1.0), the dimensional increase in the density of the enriched mantle component is 138.75 kg/m^3, 157.25 kg/m^3 and 185 kg/m^3, respectively, for a comparison of surface temperature materials (equating with density increases of 3.75%, 4.25% and 5%). However, these contrasts must be adjusted when temperature contrast between the CAID and ambient mantle material is considered. Moreover, in the lowermost mantle, the thermal expansion coefficient may be up to 50% lower than its upper mantle value. As illustrated in Fig. 2, the dense provinces are typically 1000-1250 K (0.4 to 0.5ΔT) hotter than the ambient mantle, so that thermal influence, combined with a reduction in the thermal expansion coefficient, reduces their density contrast when compared to the ambient mantle (assuming a thermal expansion coefficient of 1×10^{-5} K^{-1} and an ambient mantle nondimensional temperature of 0.5). Accordingly, the CAID material provinces modelled are thus approximately 0.625% to 1.5% more dense than the adjacent mantle at the same depth. Actual density anomalies associated with the LLSVPs remain an issue of debate (e.g., McNamara, 2019), but may be encompassed within this range. However, in these models, the primary factor that determines the choice of the intrinsic density contrast between the enriched and ambient mantle components is ultimately the requirement of the durability of the denser volume of the two-component system. For models in which the denser component is not replenished, such as in this study, the specification of a buoyancy number below 0.7 results in entrainment and mixing of the dense layer given vigorous convection persisting over time periods of a few billion years. Our calculations (and the implied minimum and maximum density anomaly they yield between the ambient mantle and chemically distinct regions) result in a density anomaly estimate that is consistent with that inferred from seismic observations (Trampert et al. 2004).

Our study imposed the requirement that plate-like surface motion should be exhibited for calculations producing LLSVP-type piles on the CMB, if model outcome is to be considered applicable to understanding the feedback between surface dynamics and the Earth's deep interior. This requirement is especially important because plate-like surface behaviour produces strong focussed downwellings in the mantle (slabs) and these features have the greatest impact on the distribution and mobility of the CAID material (e.g., McNamara & Zhong, 2005; Zhang et al., 2010). However, the simultaneous modelling of dynamically evolving plates and thermochemical piles increases the number of variables in the system so that the cases presented here comprise coverage of a small fraction of the possible cases that may be relevant to Earth's evolution. Despite this, some specific behaviour appears to be general. A small number of thermochemical piles are not readily obtained in the 3D calculations. Instead, downwelling sheets penetrate CAID material layers to produce a distribution better described as a layer punctuated by multiple holes. Decreasing the volume of the CAID material tends to reduce the mean thickness of the layer featuring the holes rather than prompting the separation of the dense material into piles. Moreover, decreasing the volume of the dense component is contrary to non-consensus estimates of the volume of the LLSVPs which are as great as eight percent of the mantle's volume (Cottaar & Lekic, 2016). As described by numerous other authors, decreasing the buoyancy number of the denser component can allow for the formation of higher topography, reduced 'footprint' piles, but this occurs at the expense of pile durability. In the models we present, which assume a primordial, non-renewing, CAID component, a lower buoyancy number is conducive to mixing and dissipation of the dense component (e.g., Trim et al., 2020). Possible future avenues for investigation that may reconcile the existence of two thermochemical piles in a spherical shell exhibiting plate tectonics may require the modelling of a renewing source lower buoyancy number material for the CAID component than was consider in this study. However, this may be problematic (Brandenburg & van Keken, 2007; Li & McNamara, 2013) rather than offering a solution. Nakagawa et al. (2010) and Nakagawa & Tackley (2011) employed sophisticated three-dimensional spherical models in which the dense material was produced by melting but also did not obtain two piles in the systems studied.

In contrast, studies that have imposed plate velocity on 3D spherical shells have readily obtained two LLSVP-like features for anomalously dense mantle components similar in volume, relative density and viscosity to those investigated here. The difference in our findings and those of investigations that imposed recent plate motion history (e.g., McNamara & Zhong, 2005; Zhang et al., 2010) may result from a lack of feedback in the former studies but could also stem from the neglect of continents in the work presented here. The breakup of a supercontinent might impact the number of piles obtained in the deep mantle. For example, dispersing continents (or the process of supercontinent breakup) may play a role in organizing subduction in a way that results in a dominant degree-2 convection pattern that simultaneously promotes two thermochemical provinces (e.g., Li & Zhong, 2009; Li & Zhong, 2017). However, exploring the feedback between a CAID component, continents and the modelling of dynamic oceanic plates remains a computational challenge in 3D systems with Earth-like convective vigour so that studies will be strongly limited by the number of variables that can be investigated.

Despite the difficulty of obtaining two LLSVP-like provinces from the addition of a CAID component to a 3D model, two-dimensional components not only readily produce two distinct piles but can also emulate some of the other seismically inferred morphology. For example, at time 1.58 Gyr in Fig. 5, the calculation featuring a buoyancy number of 0.75 exhibits one province that rises approximately 1000 km above the CMB while the other province is just half that height. Together the provinces cover about 30% of the CMB. These figures mimic the approximate dimensions of the LLSVPs determined by seismic studies, including the greater volume and height of the African anomaly (e.g., Cottaar & Lekic, 2016). In general, the time-dependence of the CAID material features in the 2D calculations take on a variety of shapes that can mimic cross-sections of LLSVP images. Specifically, the intrinsically dense provinces are more likely to take on heights in excess of 1000 km or more above the CMB when the buoyancy number is in the 0.75 - 0.85 range and the intrinsic viscosity contrast between the enriched and surrounding material is much greater than one. However, we note that we model a uniform distribution of internal heat sources. For higher buoyancy number, enrichment of the CAID material with a greater degree of internal heating (e.g., Li et al., 2019) could produce higher topography features than those found in our study. Nevertheless, the findings presented from this study are cautionary, in that they show that conclusions regarding the physical properties of the LLSVPs, inferred from the morphology of dense components in 2D thermochemical models do not always reproduce LLSVP-like features in 3D systems.

A similar issue exists with regard to modelling plates in the presence (or absence) of a two-component lower mantle. The modelling of plates affects system heat flow at both the upper and lower boundaries. Dramatically different system behaviour is therefore possible in models featuring the modelling of plates, when the heating conditions are identical. For example, the presence of a CAID component partially blanketing the CMB reduces heat flow into the mantle and therefore results in a cooler interior. The result of a cooler mantle is analogous to reducing the internal heating rate of the mantle, which has been shown in multiple studies employing plate modelling methods (e.g., Stein et al., 2014) to promote surface mobility. Similarly, the presence of a CAID component in the lower mantle can affect the formation of plate boundaries because of the impact of reduced mantle temperature on the tractions that break the model lithosphere. In addition, the two-dimensional calculations in our study showed not only that slabs could impact, deform and split CAID material provinces but that the provinces would instil convective patterns that would result in repeated failure of the lithosphere in the same narrow region. Thus, the modelling of plates and the inclusion of a CAID mantle component results in a feedback that appears to affect both CAID material distribution and plate boundary locations. A potential disruption to the establishment of such feedback might be provided by the inclusion of continents in these models or the change in the limited degree of freedom for plate motion that accompanies three-dimensionality. Accordingly, we conclude that the physical properties of a CAID mantle component that will promote the formation of a pair of distinct provinces may require the modelling of continents covering about 30% of the mantle's surface.

5 Conclusion

Tectonic plate motion has been a corollary of terrestrial mantle convection (e.g., Bercovici, 2003; Coltice et al., 2017; 2019; Crameri et al., 2019) for more than a billion years (Dhuime et al., 2015). Consequently, investigating the evolution of the current structure of the deep interior with global-scale mantle convection calculations requires modelling a system yielding the primary aspects of plate tectonics: the existence of focussed sheet-like downwellings (slabs), persistent piece-wise uniform surface motion, and the presence of evolving plate boundaries. Previous work has shown that mantle convection models featuring methods for reproducing or generating plate-like surface velocity fields (e.g., Monnereau & Quéré, 2001; Lowman et al., 2001; Lenardic et al., 2019) exhibit internal temperature structure (and therefore viscosity) that differs from systems with other surface behaviour. Principally, this effect is produced by the influence that plates have on mantle heat loss. The presence of chemically dense provinces lying on the core mantle boundary have been shown (Langemeyer et al., 2020) to inhibit heat flow into the mantle and therefore also affect mantle temperatures (and viscosity). Here we show that for modest volumes (2-3.5% of the mantle) the impact of incorporating a compositionally anomalous and intrinsically dense component in mantle convection calculations can change temperature profiles so that plate-like surface behaviour is obtained for different parameter values from those required for isochemical models.

Presenting results from eleven vigorously convecting 3D calculations, we also show that obtaining a pair of compositionally distinct provinces with LLSVP-like coverage of the CMB is elusive in systems featuring dynamically evolving plate-like surfaces. Not only does the presence of a CAID component in the mantle affect the surface velocity field character, but a pair of enduring provinces did not evolve in any of the cases that we considered. In contrast, two-dimensional systems exhibit a pair of diametrically opposed provinces for a range of model parameters. We highlight the significance of flow direction in explaining this discrepancy. The CAID material in a 2D model can only flow in two lateral directions. Accordingly, slab impact above a dense province inevitably divides the existing feature into two detached components and drives the resulting features in opposing directions. The additional degrees of freedom in a 3D calculation allow for flow of the CAID material to move so that the intrinsically denser material can become perforated by the arrival of a slab but not necessarily divided. Moreover, a mass of CAID material can be split from a perimeter location inwards to a radial hinge-point, around which the material will effectively rotate in a nearly horizontal plane while never separating into two detached masses.

The cases we present here are far from exhaustive in terms of the values considered for CAID material density contrast or viscosity contrast. Similarly, the values specified in our calculations for the key parameters governing plate formation represent a small subset from just one possible rheological description of mantle flow. However, the findings illustrate a few fundamental issues that are likely to prevail in further studies. Namely, the obtaining of LLSVP-type features from thermochemical mantle components is not an inevitable system outcome, particularly when a simultaneous requirement for a plate-like surface is also imposed; the inclusion of a CAID component in a model can be either conducive to encouraging the generation of a plate-like surface velocity field or detrimental to producing plates; and intrinsically dense mantle components may remain rooted in the deep mantle while trapping enough heat within so that their relative contrast in density (and viscosity) with the surrounding mantle is much less than implied by the comparative properties at a common temperature.

Acknowledgments

The authors thank M. Li and an anonymous reviewer for constructive comments on the original manuscript. S.M.L. and J.P.L are grateful for funding from the NSERC of Canada (grant: 327084-10). Computations were performed on the Niagara supercomputer at the SciNet HPC Consortium. SciNet is funded by: the Canada Foundation for Innovation; the Government of Ontario; Ontario Research Fund - Research Excellence; and the University of Toronto.

Code Availability

The computer code, STAGYY, used for all calculations described herein can be obtained upon reasonable request from P.J. Tackley.

References

Amit, H., Olson, P., 2015. Lower mantle superplume growth excites geomagnetic reversals, *Earth Planet. Sci. Lett.*, **414**, 68-76, doi:10.1016/j.epsl.2015.01.013.

Auer, L., Boschi, L., Becker, T.W., Nissen-Meyer, T., Giardini, D., 2014. Savani: A variable resolution whole-mantle model of anisotropic shear velocity variations based on multiple data sets, *J. Geophys. Res. Solid Earth*, **119**(4), 3006–3034, doi:10.1002/2013JB010773.

Ballmer, M.D., Houser, C., Hernlund, J.W., Wentzcovitch, R.M., Hirose, K., 2017. Persistence of strong silica-enriched domains in the Earth's lower mantle, *Nature Geosci.*, **10**, 236–240.

Bercovici, D., 2003. The generation of plate tectonics from mantle convection, *Earth Planet. Sci. Lett.*, **205**(3-4), 107-121.

Boehler, R., 2000. High pressure experiments and the phase diagram of lower mantle and core materials. *Reviews of Geophysics*, **38**(2), 221–245.

Boyet, M., Carlson, R.W., 2006. A new geochemical model for the Earth's mantle inferred from 146 sm–142 nd systematics, *Earth Planet. Sci. Lett.*, **250(1)**, 254–268, doi:10.1016/j.epsl.2006.07.046.

Brandenburg, J.P., van Keken, P.E., 2007. Deep storage of oceanic crust in a vigorously convecting mantle, *J. Geophys. Res. (SE)*, **112**(B6), doi:10.1029/2006JB004813.

Burke, K., Torsvik, T.H., 2004. Derivation of large igneous provinces of the past 200 million years from long-term heterogeneities in the deep mantle, *Earth Planet. Sci. Lett.*, **227 (3–4)**, 531–538.

Burke, K., Steinberger, B., Torsvik, T.H., Smethurst, M.A., 2008. Plume generation zones at the margins of large low shear velocity provinces on the core-mantle boundary, *Earth Planet. Sci. Lett.*, **265**, 49–60, doi:10.1016/j.epsl.2007.09.042.

Coltice, N., Gérault, M., Ulvrová, M., 2017. A mantle convection perspective on global tectonics, *Earth Sci. Rev.*, **165**, 120-150.

Coltice, N., Husson, L., Faccenna, C., Arnould, M., 2019. What drives tectonic plates?, *Sci Adv.*, **5**(10), doi:10.1126/sciadv.aax4295.

Cottaar, S., Lekic, V., 2016. Morphology of seismically slow lower-mantle structures, *Geophys. J. Int.*, **207**(2), 1122-1136.

Crameri, F., Conrad, C.P., Montesi, L. Lithgow-Bertelloni, C.R., 2019. The dynamic life of an oceanic plate, *Tectonophys.*, **760**(5), 107-135, doi:10.1016/j.tecto.2018.03.016.

Davies, D., Goes, S., Lau, H., 2015. Thermally dominated deep mantle LLSVPs: A review, in The Earth's Heterogeneous Mantle, edited by A. Khan and F. Deschamps, pp. 441–477, Springer, Switzerland, doi:10.1007/978-3-319-15627-9-14.

Deschamps, F., Kaminski, E., Tackley, P.J., 2011. A deep mantle origin for the primitive signature of ocean island basalt, *Nat. Geosci.*, **4(12)**, 879–882, doi:10.1038/ngeo1295.

Dhuime, B., Wuestefeld, A., Hawkesworth, C.J., 2015. Emergence of modern continental crust about 3 billion years ago, *Nature Geoscience*, **8**, 552–555.

Dziewonski, A.M., Lekic, V., Romanowicz, B.A., 2010. Mantle anchor structure: An argument for bottom up tectonics, *Earth Planet. Sci. Lett.*, **299(1)**, 69–79, doi:10.1016/j.epsl.2010.08.013.

Flament, N., Williams, S., Müller, R.D., Gurnis, M., Bower, D.J., 2017. Origin and evolution of the deep thermochemical structure beneath Eurasia, *Nat. Commun.* **8**, 14164, doi:10.1038/ncomms14164.

Garnero, E.J., McNamara, A.K., Shim, S.-H., 2016. Continent-sized anomalous zones with low seismic velocity at the base of the Earth's mantle, *Nature Geosci.*, **9**, doi:10.1038/ngeo2733.

Garnero, E.J., McNamara, A.K., 2008. Structure and dynamics of Earth's lower mantle, *Science*, **320**, 626–628, doi:10.1126/science.1148028.

Gurnis, M., 1988. Large-scale mantle convection and the aggregation and dispersal of supercontinents, *Nature*, **332**(6166), 695–699, doi:10.1038/332695a0.

Hager, B.H., 1984. Subducted slabs and the geoid: Constraints on mantle rheology and flow, *J. Geophys. Res.*, **89**(B7), 6003–6015. https://doi.org/10.1029/JB089iB07p06003

Hansen, U., D.A. Yuen, 1989. Dynamical influences from thermal-chemical instabilities at the core-mantle boundary, *Geophys. Res. Lett.*, 16(7), 629-632.

Hernlund, J.W., Houser, C., 2008. On the statistical distribution of seismic velocities in Earth's deep mantle, *Earth Planet. Sci. Lett.*, **265(3-4)**, 423-437, doi:10.1016/j.epsl.2007.10.042.

Heyn, B.H., Conrad, C.P., Tronnes, R.G., 2020. How thermochemical piles can (periodically) generate plumes at their edges, *J. Geophy. Res. Solid Earth*, doi:10.1029/2019JB018726.

Heyn, B.H., Conrad, C.P., Tronnes, R.G., 2018. Stabilizing effect of compositional viscosity contrasts on thermochemical piles, *Geophys. Res. Lett.*, doi:10.1029/2018GL078799.

Höink, T., Lenardic, A., Richards, M., 2012. Depth-dependent viscosity and mantle stress amplification: implications for the role of the asthenosphere in maintaining plate tectonics, *Geophys. J. Int.*, **191**, 30-41, doi:10.1111/j.1365-246X.2012.05621.x.

Humayun, M., Qin, L., Norman, M.D., 2004, Geochemical evidence for excess iron in the mantle beneath Hawaii, *Science*, **306**, 91–94, doi:10.1126/science.1101050.

Ishii, M., Tromp, J., 1999. Normal-mode and free-air gravity constraints on lateral variations in velocity and density of Earth's mantle, *Science*, **285**, 1231–1236, doi:10.1126/science.285.5431.1231.

King, S.D., Masters, G., 1992. An inversion for radial viscosity structure using seismic tomography, *Geophys. Res. Lett.*, **19**(15), 1551–1554, doi:10.1029/92GL01700.

Koelemeijer, P., Deuss, A., Ritsema, J., 2017. Density structure of Earth's lowermost mantle from Stoneley mode splitting observations, *Nature Comm.*, **8**, 15241.

Koglin, D.E., Ghias, S.R., King, S.D., Jarvis, G.T., Lowman, J.P., 2005. Mantle convection with reversing mobile plates: A benchmark study, *Geochem. Geophys. Geosys.*, **6**, Q09,003, doi:10.1029/2005GC000924.

Labrosse, S., Hernlund, J., Coltice, N., 2007. A crystallizing dense magma ocean at the base of the Earth's mantle, *Nature*, **450**, 866–869, doi:10.1038/nature06355.

Langemeyer, S.M., Lowman, J.P., Tackley, P.J., 2018. The sensitivity of core heat flux to the modeling of plate-like surface motion, *Geochem. Geophys. Geosyst. (Gcubed)*, **19**, 1282-1308, doi:10.1002/2017GC007266.

Langemeyer, S.M., Lowman, J.P., Tackley, P.J., 2020. The dynamics and impact of compositionally originating provinces in a mantle convection model featuring rheologically obtained plates, *Geophys. J. Int.*, **220(3)**, 1700-1716, doi:10.1093/gji/ggz497.

Langemeyer, S.M., Lowman, J.P., Tackley, P.J., 2021. Global mantle convection models produce transform offsets along divergent plate boundaries, *Commun Earth Environ*, **2** 69, https://www.nature.com/articles/s43247-021-00139-1.

Lau, H.C.P., Mitrovica, J.X., Davis, J.L., Tromp, J., Yang, H.Y., Al-Attar, D., 2017. Tidal tomography constrains Earth's deep-mantle buoyancy, *Nature*, **551**, 321–326.

Lay, T., Hernlund, J., Buffett, B. A., 2008. Core-mantle boundary heat flow, *Nature Geosci.*, **1(1)**, 25-32. doi:10.1038/ngeo.2007.44, http://dx.doi.org/10.1038/ngeo.2007.44.

Le Bars, M., Davaille, A., 2004. Large interface deformation in two-layer thermal convection of miscible viscous fluids, *J. Fluid Mech.*, **499**, 75-110.

Lekic, V., Cottaar, S., Dziewonski, A.M., Romanowicz, B., 2012. Cluster analysis of global lower mantle tomography: a new class of structure and implications for chemical heterogeneity *Earth Planet. Sci. Lett.*, 357–358 **68**, 77.

Lenardic, A., Weller, M., Höink, T., Seales, J., 2019. Toward a boot strap hypothesis of plate tectonics: Feedbacks between plates, the asthenosphere, and the wavelength of mantle convection, *Phys. Earth Planet. Int.*, **296**, doi:10.1016/j.pepi.2019.106299.

Li, M., McNamara, A.K., 2013. The difficulty for subducted oceanic crust to accumulate at the Earth's core-mantle boundary, *J. Geophys. Res. (SE)*, **118**(4), 1807-1816, doi:10.1002/jgrb.50156.

Li, M., Zhong, S., Olson, P., 2018. Linking lowermost mantle structure, core-mantle boundary heat flux and mantle plume formation, *Phys. Earth Planet. Int.*, **277**, 10-29, doi:10.1016/j.pepi.2018.01.010.

Li, M., Zhong, S., 2017. The source location of mantle plumes from 3D spherical models of mantle convection, *Earth Planet. Sci. Lett.*, **478**, 47-57, doi:10.1016/j.epsl.2017.08.033.

Li, Z.-X., Zhong, S., 2009. Supercontinent-superplume couplng. true-polar wander and plume mobility: plate dominance in whole mantle tectonics, *Phys. Earth Planet. Int.*, **176**, 143-156.

Li, Y., Deschamps, F., Tackley, P.J., 2014. The stability and structure of primordial reservoirs in the lower mantle: insights from models of thermochemical convection in three-dimensional spherical geometry, *Geophys. J. Int.*, **199**, 914-930, doi: 10.1093/gji/ggu295.

Li, Y., Deschamps, F., Yang, J., Chen, L., Zhao, L., Tackley, P.J., 2019. Effects of the compositional viscosity ratio on the long-term evolution of thermochemical reservoirs in the deep mantle, *Geophys. Res. Lett.*, **46**(16), 9591-9601, doi:10.1029/2019GL083668.

Lowman, J.P., King, S.D., Gable, C.W., 2001. The influence of tectonic plates on mantle convection patterns, temperature and heat flow, *Geophys. J. Int.*, **146**, 619-636.

Masters, G., Laske, G., Bolton, H., Dziewonski, A., 2000. The relative behaviour of shear velocity, bulk sound speed, and compressional velocity in the mantle: implications for chemical and thermal structure, *Geophys. Monogr. Ser. Am. Geophys. Un.* **117**, 63-88.

McNamara, A.K., 2019. A review of large low shear velocity provinces and ultra low velocity zones, *Tectono.*, **760**, 199-220.

McNamara, A.K., Zhong, S., 2005. Thermochemical structures beneath Africa and the Pacific Ocean, *Nature*, **437** 7062, 1136-1139.

McNamara, A.K., Zhong, S., 2004. Thermochemical structures within a spherical mantle: Superplumes or piles?, *J. Geophys. Res.*, **109**, B07402, doi:10.1029/2003JB002847.

Mitrovica, J.X., Forte, A.M., 2004. A new inference of mantle viscosity based upon joint inversion of convection and glacial isostatic adjustment data, *Earth. Planet. Sci. Lett.*, **225**, 177-189, doi:10.1016/j.epsl.2004.06.005.

Monnereau, M., Quéré, S., 2001. Spherical shell models of mantle convection with tectonic plates, *Earth Planet. Sci. Lett.*, 184(3), 575–587, doi:10.1016/S0012-821X(00)00334-4.

Moulik, P., Ekström, G., 2016. The relationships between large-scale variations in shear velocity, density, and compressional velocity in the Earth's mantle, *J. Geophys. Res. (Solid Earth)*, **121**, 2737-2771, doi.org/10.1002/2015JB012679.

Murphy, J.B., Nance, R.D., 2004. How do supercontinents assemble?, *Amer. Scient.*, **92**, 324-333.

Nakagawa, T., Tackley, P.J., 2011. Effects of low-viscosity post-perovskite on thermo-chemical mantle convection in a 3-D spherical shell, *Geophys. Res. Lett.*, **38**(4), doi:10.1029/2010GL046494.

Nakagawa, T., Tackley, P.J., Deschamps, F., Connolly, J.A.D., 2010. The influence of MORB and harzburgite composition on thermo-chemical mantle convection in a 3-D spherical shell with self-consistently calculated mineral physics, *Earth Planet. Sci. Lett.*, **296**(3)-(4), 403-412, doi.org/10.1016/j.epsl.2010.05.026.

Ni, S., Tan, E., Gurnis, M., Helmberger, D., 2002. Sharp sides to the African superplume, *Science*, **296**(5574), 1850–1852,doi:10.1126/science.1070698

Richards, M.A., Hager, B.H., 1984. Geoid anomalies in a dynamic Earth. *J. Geophys. Res.*, **89**(B7), 5987–6002. https://doi.org/10.1029/JB089iB07p05987

Ritsema, J., Ni, S., Helmberger, D.V., Crotwell, H.P., 1998. Evidence for strong shear velocity reductions and velocity gradients in the lower mantle beneath Africa, *Geophys. Res. Lett.*, **25**(23), 4245–4248, doi:10.1029/1998GL900127.

Rolf, T., Coltice, N., Tackley, P.J., 2012. Linking continental drift, plate tectonics and the thermal state of the Earth's mantle, *Earth Planet. Sci. Lett.*, **351-352**, 134-146, doi:10.1016/j.epsl.2012.07.011.

Schuberth, B.S.A., Bunge, H.-P., Ritsema, J., 2009. Tomographic filtering of high-resolution mantle circulation models: Can seismic heterogeneity be explained by temperature alone?, *Geochem. Geophys. Geosyst.*, **10**, Q05W03, doi:10.1029/2009GC002401.

Schuberth, B.S.A., Zaroli, C., Nolet, G., 2012. Synthetic seismograms for a synthetic Earth: Long-period P- and S-wave traveltime variations can be explained by temperature alone, *Geophys. J. Int.*, **188**(3), 1393–1412, doi:10.1111/j.1365-246X.2011.05333.x.

Stein, C., Martens, M., Hansen, U., 2020. A numerical study of thermal and chemical structures at the core-mantle boundary, *Earth Planet. Sci. Lett.*, **548**, doi:10.1016/j.epsl.2020.116498.

Stein, C., Lowman, J.P., Hansen, U., 2014. A comparison of mantle convection models featuring plates, *Geochem. Geophys. Geosyst.*, *15*, doi:10.1002/2013GC005211.

Stein, C., Hansen, U., 2008. Plate motions and the viscosity structure of the mantle — Insights from numerical modelling, *Earth Planet. Sci. Lett.*, **272**(1-2), 29-40, doi:10.1016/j.epsl.2008.03.050.

Stein, C., Schmalzl, J., Hansen, U., 2004. The effect of rheological parameters on plate behaviour in a self-consistent model of mantle convection, Phys. Earth Planet. Int.,

142(3–4), 225-255.

Su, W.-J., Dziewonski, A., 1997. Simultaneous inversions for 3-D variations in shear and bulk velocity in the mantle, *Phys. Earth Planet. Inter.*, **100**, 135-156.

Tackley, P. J., 1998. Three-dimensional simulations of mantle convection with a thermo-chemical CMB boundary layer: D"?, in The Core-Mantle Boundary Region, edited by M. Gurnis, M. E. Wysession, E. Knittle and B. A. Buffett, pp. 231-253, American Geophysical Union.

Tackley, P. J., King, S.D., 2003. Testing the tracer ratio method for modeling active compositional fields in mantle convection simulations. **Geochem., Geophys., Geosys.**, **4**(4), 8302. https://doi.org/10.1029/2001GC000214

Tackley, P. J., Xie, S., Nakagawa, T., Hernlund, J.W., 2005. Numerical and laboratory studies of mantle convection: Philosophy, accomplishments, and thermochemical structure and evolution, in Earth's Deep Mantle: Structure, Composition, and Evolution, **160**, edited by R. D. Van Der Hilst et al., pp. 83–99, AGU, Washington, D. C., doi:10.1029/160GM07

Tan, E., Leng, W., Zhong, S., Gurnis, M., 2011. On the location of plumes and lateral movement of thermochemical structures with highbulk modulus in the 3-D compressible mantle, *Geochem. Geophys. Geosys.*, **12**, Q07005, doi:10.1029/2011GC003665

Torsvik, T.H., Smethurst, M.A., Burke, K., Steinberger, B., 2006. Large igneous provinces generated from the margins of the large low-velocity provinces in the deep mantle, *Geophys. J. Int.*, **167**(3), 1447–1460, doi:10.1111/j.1365-246X.2006.03158.x.

Torsvik, T.H., Burke, K., Steinberger, B., Webb, S.J., Ashwal, L.D., 2010. Diamonds sampled by plumes from the core–mantle boundary. *Nature*, **466**, 352–356.

Trampert, J., Deschamps, F., Resovsky, J., Yuen, D., 2004. Probabilistic tomography maps chemical heterogeneities throughout the lower mantle, *Science*, **306**(5697), 853–856, doi:10.1126/science.1101996.

Trim, S.J., Heron, P.J., Stein, C., Lowman, J.P., 2014. The feedback between surface mobility and mantle compositional heterogeneity: Implications for the Earth and other terrestrial planets, *Earth Planet. Sci. Lett.*, **405**, 1–14, doi:10.1016/j.epsl.2014.08.019.

Trim, S.J., Lowman, J.P., Butler, S.L., 2020. Improving mass conservation with the tracer ratio method: application to thermochemical mantle flows, *Geochem. Geophys. Geosyst.* **22**, doi:10.1029/2019GC008799.

Trim, S.J., Lowman, J.P., 2016. Interaction between the supercontinent cycle and the evolution of intrinsically dense provinces in the deep mantle, *J. of Geophys. Res. (Solid Earth)*, **121**(12), 8941-8969.

To, A., Romanowicz, B., Capdeville, Y., Takeuchi, N., 2005. 3D effects of sharp boundaries at the borders of the African and Pacific superplumes: Observation and modeling, *Earth Planet. Sci. Lett.*, **233**(1–2), 137–153, doi:10.1016/j.epsl.2005.01.037.

Yamazaki, D., Karato, S., 2001. Some mineral physics constraints on the rheology and geothermal structure of Earth's lower mantle, *American Mineralogist*, **86**(4), 385–391, doi: https://doi.org/10.2138/am-2001-0401.

Zhang, N., Zhong, S., Leng, W., Li, Z.-X., 2010. A model for the evolution of the Earth's mantle structure since the early Paleozoic, *J. Geophys. Res.*, **115**, B06401, doi:10.1029/2009JB006896.

Zhong, S., Gurnis, M., 1993. Dynamic feedback between a continentlike raft and thermal convection, *J. Geophys. Res.*, **98**(B7), 12219-12232, doi:10.1029/93JB00193.

Supplementary Figures: Contrasts in two- and three-dimensional system behaviour in the modelling of compositionally originating LLSVPs and a mantle featuring dynamically obtained plates

S.M. Langemeyer[1], J.P. Lowman[2], P.J. Tackley[3]

[1]Department of Physics, University of Toronto, Toronto M5S 1A7, Canada

[2]Dept. of Physical and Environmental Sciences, University of Toronto Scarborough, Toronto, M1C 1A4, Canada

[3]Department of Earth Sciences, ETH-Zurich, Sonneggstrasse 5, 8092 Zurich, Switzerland

Corresponding author: Julian Lowman, julian.lowman@utoronto.ca

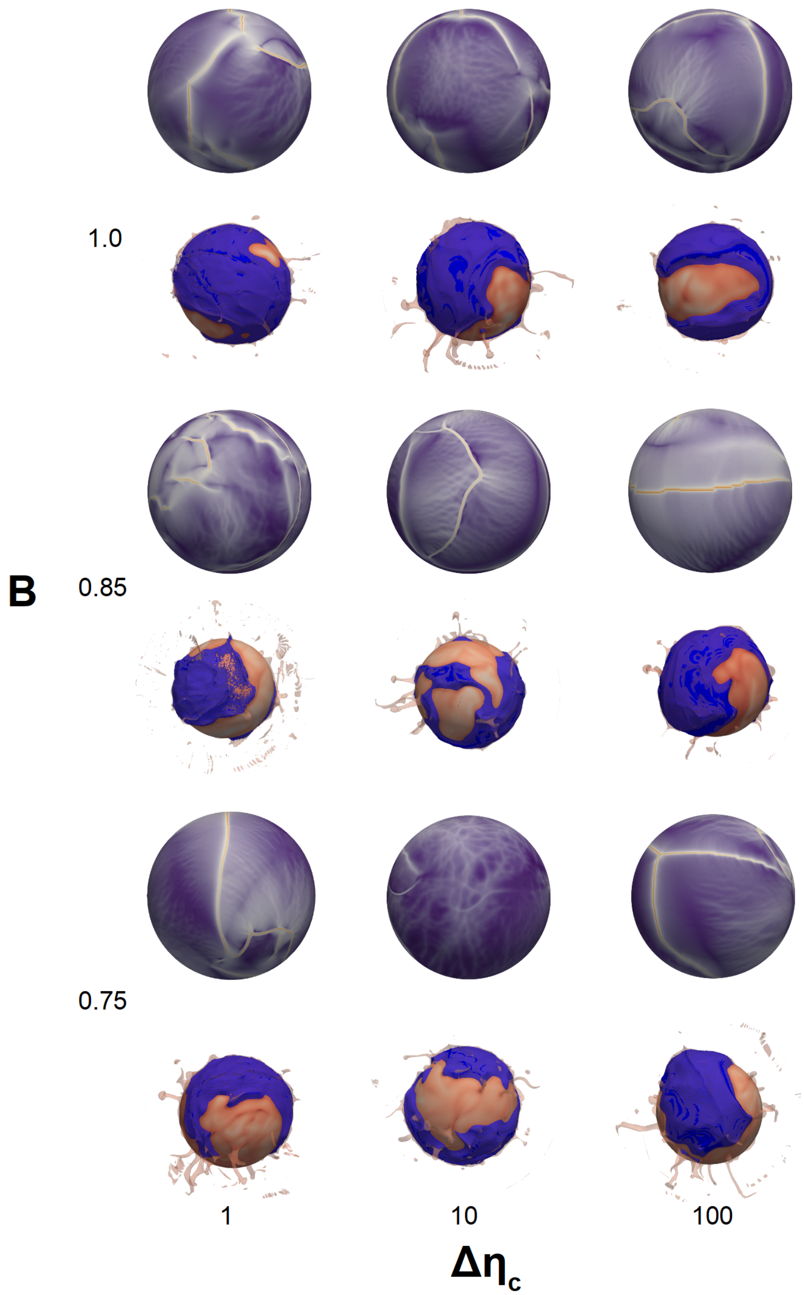

Figure 1. Snapshots of the nine uniform yield stress 3D cases featured in the study. The buoyancy number and intrinsic viscosity contrast for the CAID material and ambient mantle are indicated at the left and bottom of the figure, respectively. For each case, the viscosity field is shown at a depth of 0.005d juxtaposed with a (to scale) image of the mantle interior illustrating CAID material distribution (in blue) and thermal plumes (transparent red, non-dimensional temperature of 0.82). The viewing angle of the viscosity field and model interior pairs are the same and they are diametrically opposed to the viewing angle of the corresponding cases in Fig. 7.

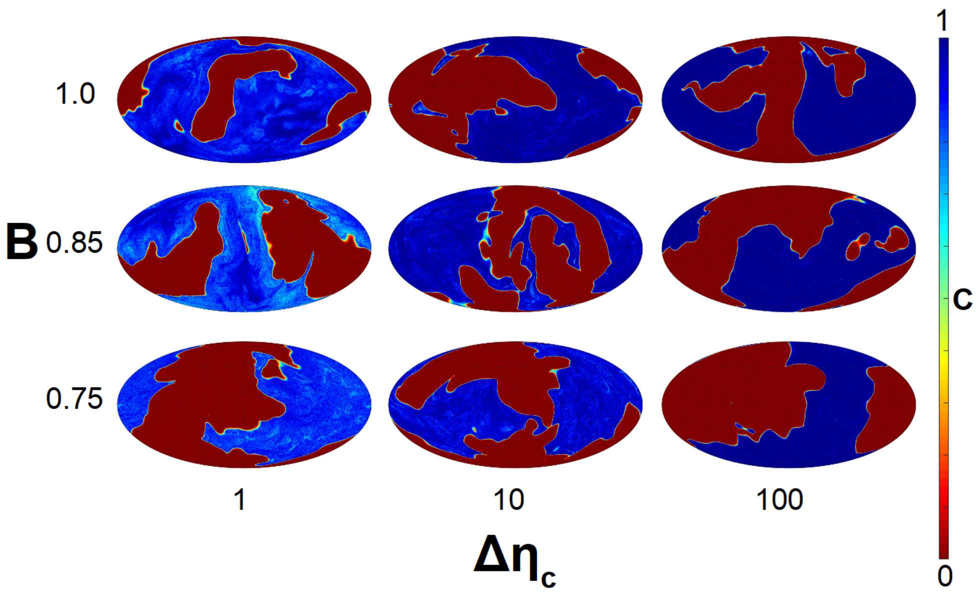

Figure 2. Mollweide projections of the composition field, C, on a surface $0.05d$ above the CMB. The panels correspond to the nine snapshots presented in Fig. 7 (and Supplementary Fig. 1). Buoyancy ratio is fixed in each row and the viscosity contrast between the intrinsically dense and ambient mantle (when both are at the CMB temperature) is fixed in each column. Blue corresponds to regions of the CMB blanketed by CAID material.

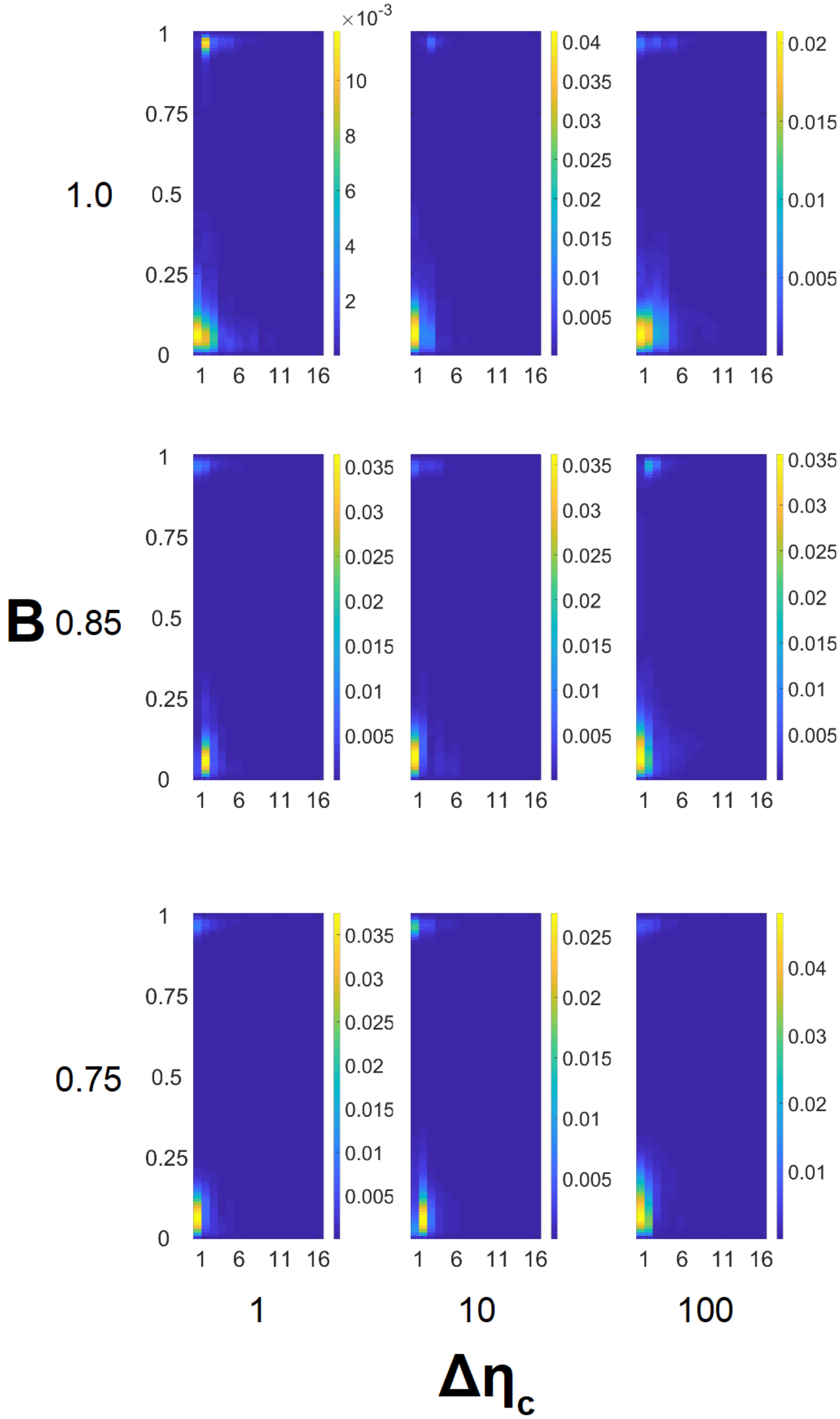

Figure 3. Power in the thermal fields presented in Fig. 7 (and Supplementary Fig. 1), as a function of spherical harmonic and non-dimensional height above the CMB.

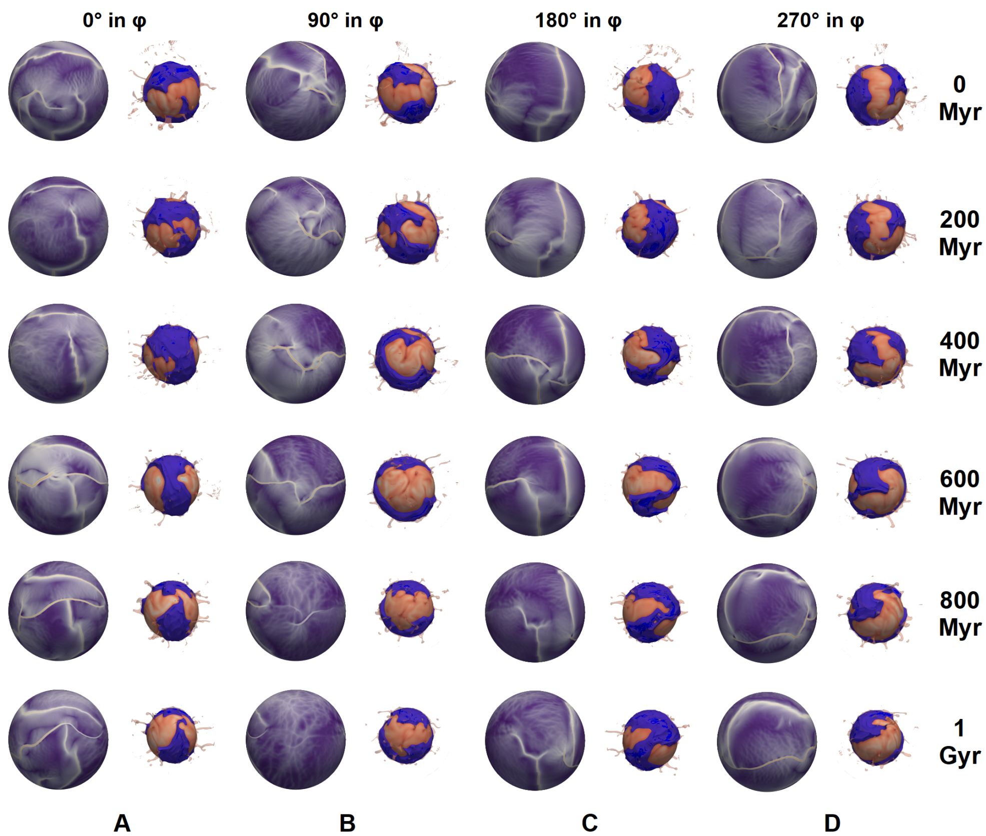

Figure 4. Snapshots of the near surface non-dimensional viscosity field and CAID material distribution at six different times (rows) throughout the evolution of Model 3DB0.75D10. The angle of rotation relative to a vertical axis through the centre of the sphere in the left-most column is indicated at the top of each column. The viewing angles used in Fig. 10 are presented for each time in the columns labelled A and C.

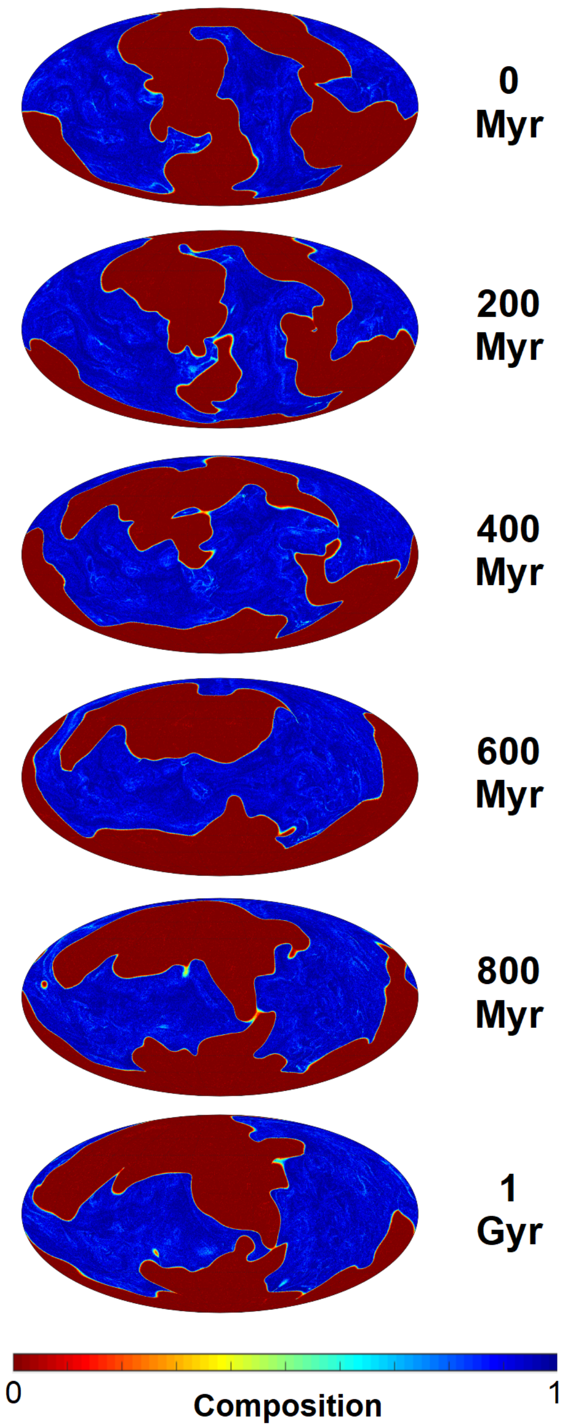

Figure 5. Mollweide projections of the composition field, C, on a surface $0.05d$ above the CMB from Model 3DB0.75D10. The panels correspond to the six snapshots presented in Fig. 10 (and Supplementary Fig. 4). Blue corresponds to regions of the CMB blanketed by CAID material.

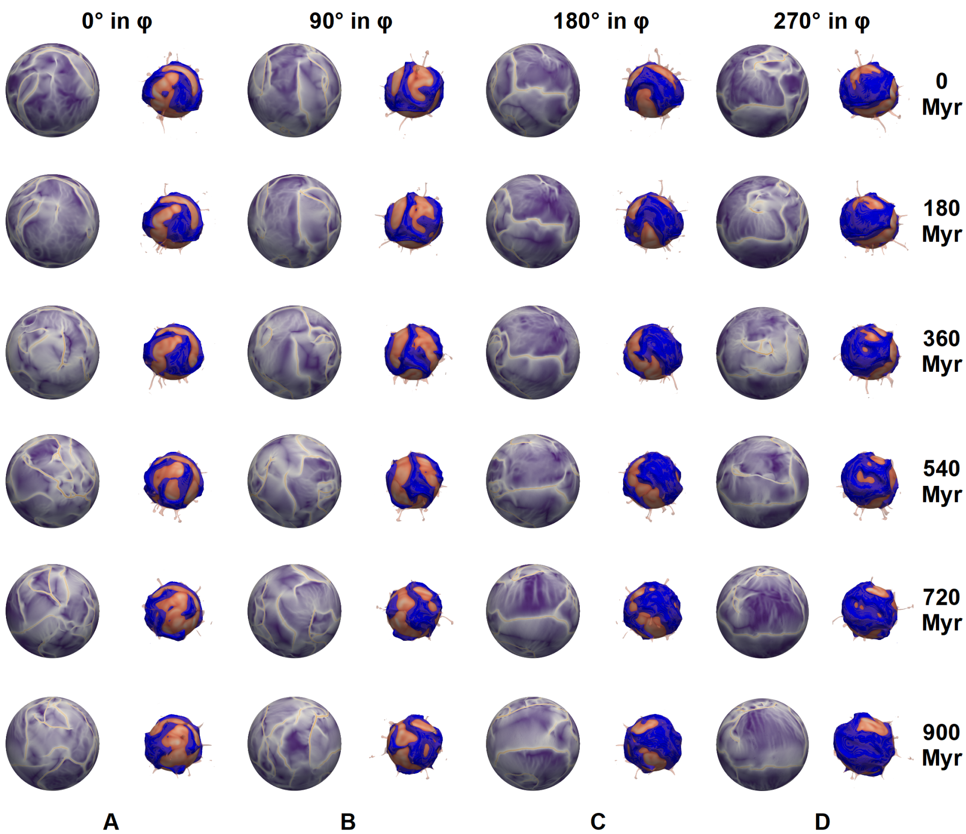

Figure 6. Snapshots of the near surface non-dimensional viscosity field and CAID material distribution at six different times (rows) throughout the evolution of Model 3DB0.75D100weak. The angle of rotation relative to a vertical axis through the centre of the sphere in the left-most column is indicated at the top of each column. The viewing angles used in Fig. 11 are presented for each time in the columns labelled A and C.

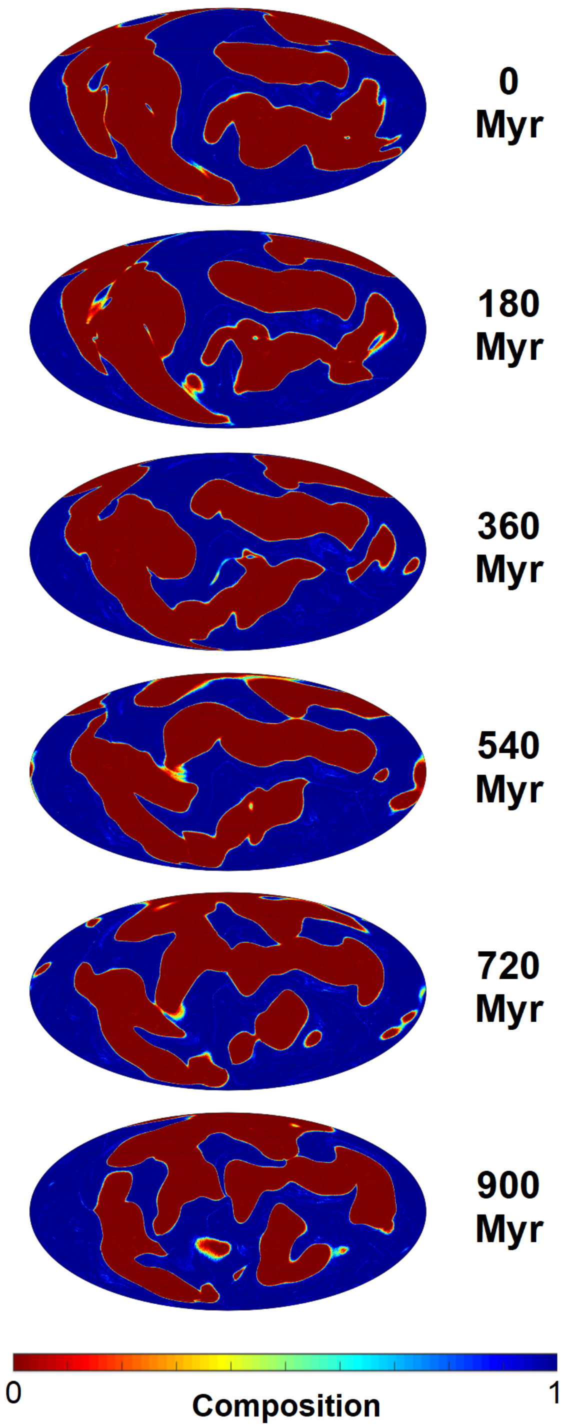

Figure 7. Mollweide projections of the composition field, C, on a surface $0.05d$ above the CMB from Model 3DB0.75D100weak. The panels correspond to the six snapshots presented in Fig. 11 (and Supplementary Fig. 6). Blue corresponds to regions of the CMB blanketed by CAID material.

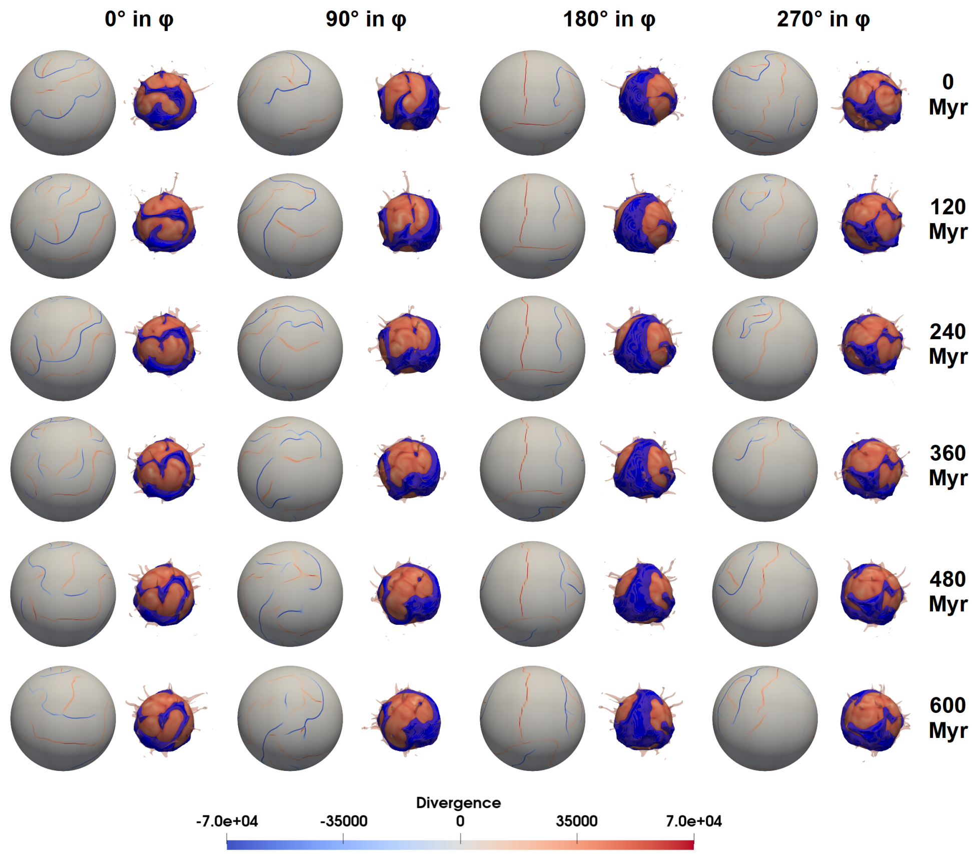

Figure 8. Snapshots of the near surface non-dimensional velocity divergence field and CAID material distribution at six different times (rows) throughout the evolution of Model 3DB0.75D100weak&reduced. The angle of rotation relative to a vertical axis through the centre of the sphere in the left-most column is indicated at the top of each column. The viewing angles used in Fig. 13 are presented for each time in the columns labelled 0° and 180°.

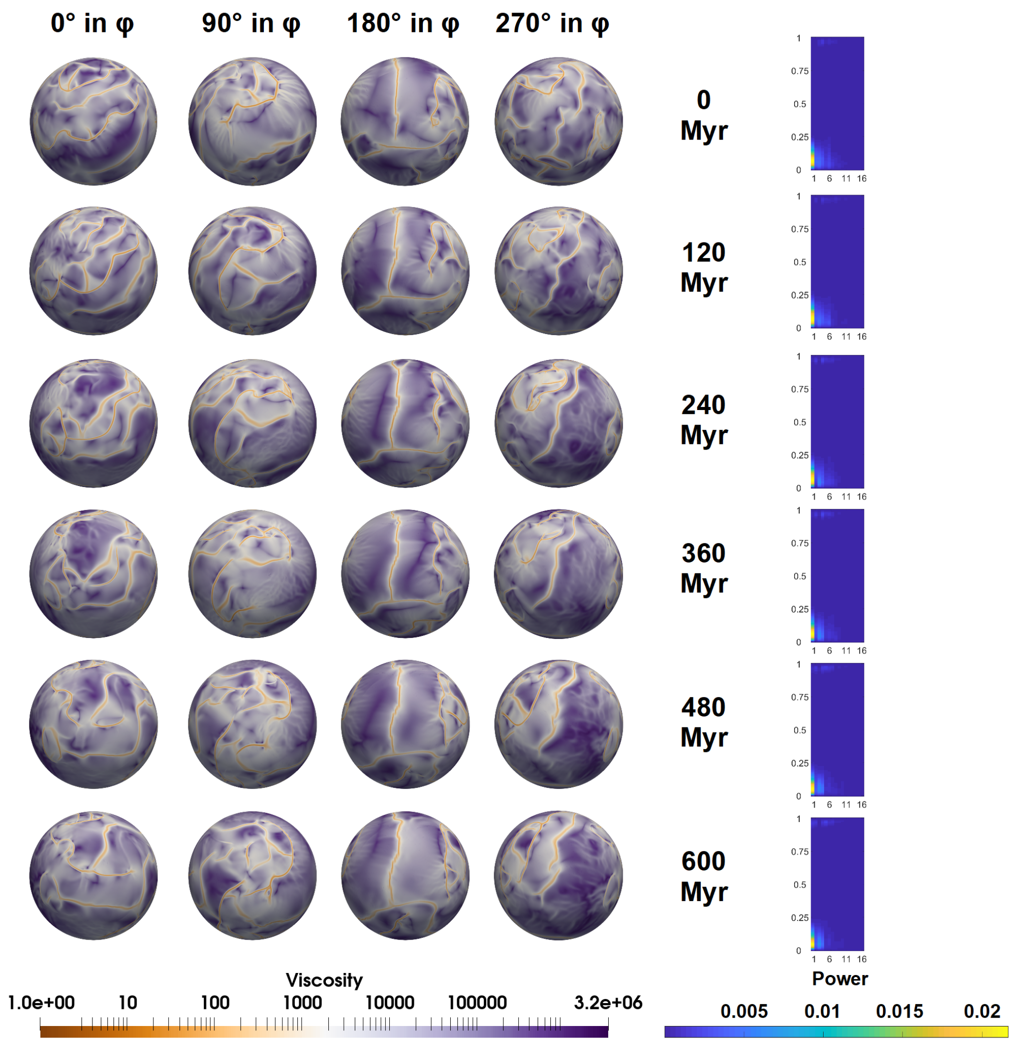

Figure 9. Snapshots of the near surface non-dimensional viscosity field and thermal power spectra at six different times (rows) throughout the evolution of Model 3DB0.75D100weak&reduced. The snapshots shown correspond to the velocity divergence field snapshots shown in Supplementary Fig. 8. The viscosity field is shown at a depth of $0.005d$. Four viewing angles are shown for each time, with the angle of rotation relative to the left most column indicated at the top of the figure. The power spectra of the temperature field at the corresponding time is shown in the right column as a function of non-dimensional height above the CMB and spherical harmonic degree.

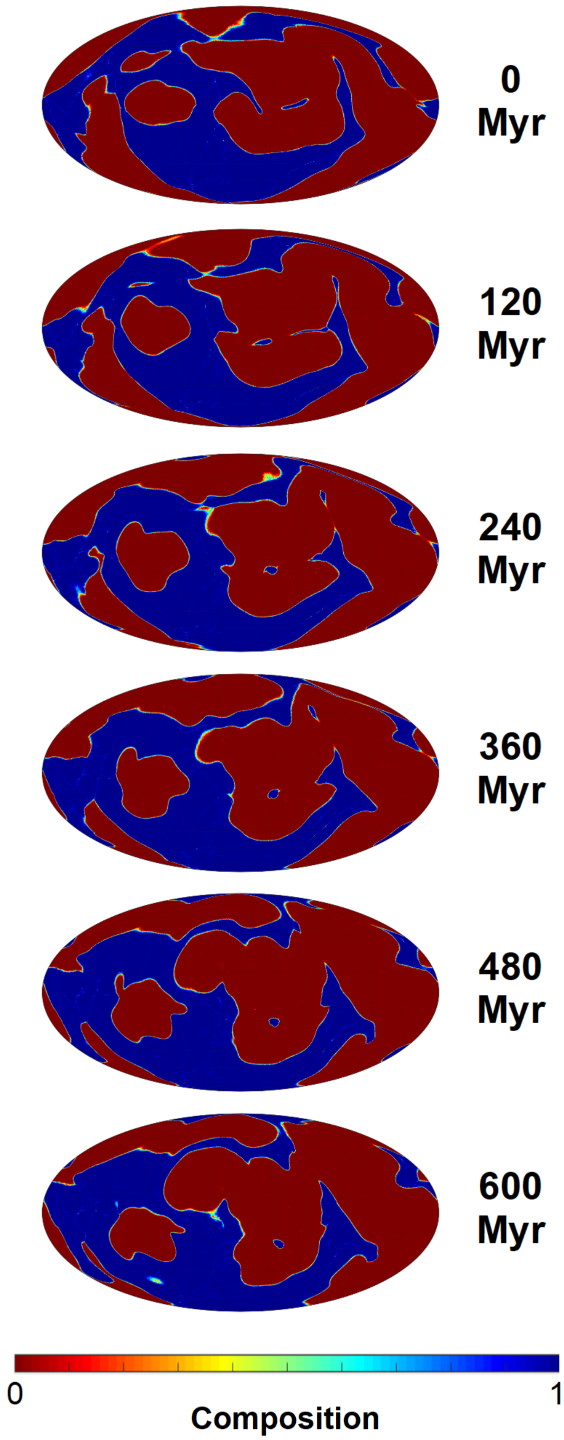

Figure 10. Mollweide projections of the composition field, C, on a surface $0.05d$ above the CMB from Model 3DB0.75D100weak&reduced. The panels correspond to the six snapshots presented in Fig. 13 (and Supplementary Fig. 8). Blue corresponds to regions of the CMB blanketed by CAID material.